

Impacts of tropical cyclones on the thermodynamic conditions in the tropical tropopause layer observed by A-train satellites

Jing Feng¹ and Yi Huang¹

¹Department of Atmospheric and Oceanic Sciences, McGill University, Montreal, Canada

Correspondence: Jing Feng (jing.feng3@mail.mcgill.ca)

Abstract.

The tropical tropopause layer (TTL) is the transition layer between the troposphere and the stratosphere. Tropical cyclones may impact the TTL by perturbing the vertical distributions of cloud, temperature, and water vapor, ~~although this impact is poorly quantified due to the lack of collocated data. To address this problem, we implement a synergistic retrieval approach to~~
5 ~~obtain the thermodynamic profiles and ice water content above thick high-level clouds using the A-Train satellite measurements that pass over the tropical cyclones.~~

~~This study detects the signature of cyclone impact. This study combines several A-Train instruments, including radar from CloudSat, lidar from Cloud-Aerosol Lidar and Infrared Pathfinder Satellite Observations (CALIPSO) satellite, and the Atmospheric InfraRed Sounder (AIRS) on Aqua satellite, to detect signatures of cyclone impacts~~
10 ~~of cloud, water vapor, temperature, and radiation by compositing these thermodynamic fields with respect relative to cyclone center locations. It is found location.~~

~~Based on the CloudSat 2B-CLDCLASS-LIDAR product, this study finds~~ that tropical cyclone events considerably increase the occurrence frequencies of TTL clouds, in the form of cirrus clouds above a clear troposphere. The amount of TTL cloud ice, however, is found to be mostly contributed by overshooting deep ~~convections that penetrate the bottom of convection that~~
15 ~~penetrates the base of the~~ TTL.

~~To overcome the lack of temperature and water vapor products in cloudy conditions, this study implements a synergistic method that retrieves temperature, water vapor, ice water content, and effective radius simultaneously by incorporating observations from AIRS, CloudSat, and CALIPSO. Using the synergistic retrieval method, we find a vertically oscillating-vertically-oscillating~~
20 ~~pattern of temperature anomalies above tropical cyclones, with warming beneath the cloud top (around 16 km) and cooling above. The atmospheric column~~ Based on water vapor profiles retrieved by the synergistic method, we find that the layer integrated water vapor above 16 km ~~is generally hydrated by overshooting convections, although dehydration is detected above non-overshooting TTL clouds. Above overshooting deep convections, the column-integrated water vapor is found to be on average 40 % higher than the climatology (LIWV) is higher above tropical cyclones, especially above overshooting deep convective clouds, compared to climatological values.~~

25 Moreover, ~~the TTL is cooled above tropical cyclones due to longwave radiative cooling~~ we find that the longwave and net radiative cooling effect of clouds prevails within 1000 km of tropical cyclone centers. The radiative heating ~~rates above cyclones~~ effects of clouds from the CloudSat 2B-FLXHR-LIDAR product are well differentiated by the collocated brightness

temperature of ~~a satellite infrared channel in the window band. Using radiative calculations, it is found~~ an infrared window channel from the collocated AIRS L1B product. By performing instantaneous radiative heating rate calculations, we further find that TTL hydration is usually associated with radiative cooling of the TTL, which inhibits the diabatic ascent of moist air ~~;~~ The across isentropic surfaces to the stratosphere. Therefore, the radiative balance of the TTL under the impact of the cyclone ~~;~~ therefore, is not in favor of maintaining the ~~does not favor the maintenance of~~ moist anomalies in the TTL or transporting water vertically to the stratosphere.

1 Introduction

35 The tropical tropopause layer (TTL, ~~located around 15-18 km~~) is the transition layer between the convective overturning circulation in the troposphere and the Brewer-Dobson circulation in the stratosphere. Once entering the TTL, air tends to rise into the stratosphere, driven by ~~the positive extratropical wave-drag and influenced by local radiative heating~~ (Holton et al., 1995; Corti et al., 2006). The clear-sky radiative heating rate above the bottom of the TTL, which is marked by the becomes positive above the level of zero radiative heating (LZRH). This level marks the altitude where the ascending motion becomes prevailing.

40 The TTL plays an important role in ~~the~~ stratosphere-troposphere exchange (Holton et al., 1995). For example, the ~~cold air at the TTL acts~~ low temperature in the TTL act as a ‘cold trap’ that modulates both the vertical and isentropic (~~horizontal~~ quasi-horizontal) transport of water vapor to the lower stratosphere (Dessler et al., 1995; Brewer, 1949; Holton and Gettelman, 2001; Gettelman et al., 2002), where water vapor, despite its low concentration, may have a large impact on radiation, climate, and atmospheric chemistry (Solomon et al., 2010; Anderson et al., 2012; Dessler et al., 2013; Huang et al., 2016).

45 Given ~~their~~ its vertical extent, deep ~~convections potentially provide~~ convection potentially provides an important pathway to transport water vapor and other constituents to the stratosphere via the TTL. Deep ~~convections~~ convection may affect the TTL in several ways. First, tropical deep ~~convections, especially the~~ convection, especially in tropical cyclones, ~~are~~ is associated with strong dynamical cooling around the tropopause level (Holloway and Neelin, 2007). Second, the injected ice and water vapor, together with the temperature anomalies caused by deep convection, can modify the radiative heating in the TTL, which
50 in turn can either speed up or slow down the upwelling motion of air and the transport to the stratosphere. Consequently, ~~the~~ air convectively injected into the TTL can be either a source or a sink of water vapor, depending on the pre-existing relative humidity (~~Jensen et al., 2007; Ueyama et al., 2018; Schoeberl et al., 2018~~) (Ueyama et al., 2018; Schoeberl et al., 2018). Simulations and observations have shown that deep ~~convections~~ convection may hydrate the upper-troposphere and lower-stratosphere (UTLS) by directly injecting water vapor and ice above mid-latitude (Anderson et al., 2012; Sun and Huang, 2015; Qu et al.,
55 2020) and tropical storms (Avery et al., 2017; Schoeberl et al., 2018), or dehydrate it by condensing the pre-existing water vapor to ice particles in ~~a supersaturated environment~~ supersaturated environments (Ueyama et al., 2018).

On the other hand, climate models and global reanalysis datasets are subject to common problems in representing ~~the~~ key processes, such as convective parameterization, (e.g., Takahashi et al., 2016), in the UTLS region. These problems include a persistent wet bias in upper tropospheric humidity (~~Huang et al., 2007; Jiang et al., 2012, 2015~~) (Huang et al., 2007; Jiang et al., 2012, 2015)
60 , discrepancies in the transportation speed of water vapor from the upper troposphere to the lower stratosphere (~~Jiang et al., 2015~~)

and the [\(Jiang et al., 2015; Schoeberl et al., 2012\) and](#) contradictory assessments of ~~diabatic heating under the impact of high clouds~~ [cloud impacts on diabatic heating](#) in the TTL region (Wright and Fueglistaler, 2013; Wright et al., 2020).

Existing satellite datasets (Waters et al., 2006; Bernath et al., 2005; Anthes et al., 2008) and aircraft campaigns (~~e.g., Jensen et al., 2013; I~~ [have advanced the \(e.g., Jensen et al., 2013; Lee et al., 2019\) have advanced](#) understanding of the TTL region, although the study of deep convective impacts on ~~the~~ temperature, water vapor, and clouds in the TTL region is still impeded by a lack of collocated measurements of these variables. The A-Train constellation (L'Ecuyer and Jiang, 2011) ~~, including Aqua, CloudSat, CALIPSO, PARASOL, and Aura,~~ carries over 20 instruments that monitor clouds and other atmospheric variables. However, the sounding of thermodynamic conditions above deep convection, especially near the convective core, remains a challenge (Livesey et al., 2017; Olsen et al., 2013). ~~Feng and Huang (2018)~~ [Feng and Huang \(2018\)](#) found that the retrievability of temperature and water vapor is improved by an underlying cloud layer because the cloud layer reduces the degeneracy caused by non-monotonic ~~temperature variation~~ [vertical temperature variations](#) and the smearing effect of lower-level water vapor, and proposed a cloud-assisted retrieval algorithm that can be applied to ~~the~~ infrared hyperspectral measurements, such as those from the Atmospheric Infrared Sounder (AIRS, Chahine et al., 2006) ~~)-~~ aboard Aqua (Parkinson, 2003). Feng et al. (2021) further developed a synergistic method that incorporates cloud measurements of collocated active cloud profilers. By conducting a simulation experiment, Feng et al. (2021) demonstrated that this method can capture the variability of temperature and humidity above tropical convective storms and improve ~~the~~ retrievals near the cloud top through the incorporation of [information from](#) active sensors.

In this study, we aim to quantify the effect of tropical cyclones on ~~the~~ TTL temperature, water vapor, and clouds using ~~the~~ A-Train satellite observations, specifically ~~the infrared hyperspectra~~ [hyperspectral infrared measurements](#) from AIRS and cloud profiles from CloudSat ~~/CALIPSO~~ [\(Stephens et al., 2008\) and CALIPSO \(Cloud, Aerosol Lidar and the Infrared Pathfinder Satellite Obser](#). Tropical cyclones are of particular interest here because they constitute a large fraction of the most energetic (overshooting) ~~convections~~ [convective clouds](#) in the tropics (Romps and Kuang, 2009) and provide vertically extended dense high clouds that enable the above-cloud temperature and humidity retrieval method developed by [Feng and Huang \(2018\) and](#) Feng et al. (2021). By using satellite observational datasets, which are introduced in Section 2, we aim to understand: 1) how tropical cyclones, especially the overshooting events, impact ~~the~~ TTL cloud occurrence and cloud ice (see Section 3.1 and 3.2), 2) whether tropical cyclones lead to an overall hydration in the TTL (see Section 3.3), and 3) how tropical cyclones affect ~~the~~ radiative heating in the TTL (Section 4). These questions are further discussed ~~and concluded~~ [together with key conclusions](#) in Section 5.

2 Data and Methodology

90 2.1 ~~Dataset~~ [Datasets](#)

Following a sun-synchronized orbit with a repeat-cycle of 16 days, the A-Train satellites cross the equator at around 1:30 pm solar time in the ascending nodes and 1:30 am in the descending nodes every day.

CloudSat (Stephens et al., 2008) uses a cloud profiling radar operating (CPR) that operates at 94-GHz to observe cloud and precipitation. Sampling along-track at every 1.1 km, each measurement this instrument has a cross-track resolution of 1.4 km and along-track resolution of 1.8 km. With a vertical resolution of around 500 m, The Cloud-Aerosol Lidar with Orthogonal Polarization (CALIOP) is a polarization lidar carried by CALIPSO that operates at 532 and 1064 nm. The sensitivities of the two instruments in detecting cloud properties differ. The lidar signals are more sensitive to particle sizes and concentrations, but not sensitive to clouds and precipitation underneath the highest cloud layers due to the strong attenuation of the lidar signals. In comparison, radar can detect the vertical structure of cloud columns but it is not sensitive to thin cirrus clouds (Comstock et al., 2002) and smaller particles in a cloud volume. Hence, it is essential to combine the lidar and radar to obtain the sensitivity to both optically thin cirrus in the TTL and optically thick deep convective clouds (DCC).

CloudSat provides several products (version P1_R05), including cloud water content (2B-CWC-RVOD), cloud classification (2B-CLDCLASS-LIDAR), radar-lidar products by merging coincident lidar pulses within the CPR footprints (Mace et al., 2009). In this study, we use the cloud classification (2B-CLDCLASS-LIDAR, Sassen et al., 2009) and radiative heating rates (2B-FLXHR-LIDAR) products (version P2_R04). In the 2B-CLDCLASS-LIDAR product, eight cloud types are classified, including cirrus, altostratus, altocumulus, stratus, stratocumulus, cumulus, nimbostratus, and deep convective clouds, depending on the vertical distribution of hydrometeors inferred from radar signal intensity and also their horizontal length scales (?). (Wang et al., 2012). DCCs are classified based on several conditions, including a vast horizontal and vertical extent, dense hydrometers (as inferred from radar reflectivity near the cloud top), and also the presence of precipitation (Wang et al., 2012). The heating rate profiles in 2B-FLXHR-LIDAR (Leuey, 2007) are derived from two-stream broadband radiative transfer calculation combining calculations combining the 2B-CWC-RO cloud water content profile in 2B-CWC, collocated CALIPSO version-3 products (Trepte et al., 2010), and atmospheric state profiles (temperature, water vapor, and ozone) from the ECMWF forecast ECMWF forecasts, which are included in the ECMWF-AUX product (Partain, 2004).

The DARDAR (raDAR/liDAR, Delanoë and Hogan, 2008, 2010) product is based on the joint retrieval of ice clouds by using radar reflectivity measurements from CloudSat and Operational CloudSat-CALIPSO synergistic algorithms have been developed to retrieve ice cloud properties (Austin et al., 2009; Deng et al., 2010; Okamoto et al., 2010; Delanoë and Hogan, 2010) and are evaluated (Deng et al., 2013; Saito et al., 2017). This study uses a DARDAR-Cloud (raDAR/liDAR; Delanoë and Hogan, 2010) product (v2.1.1). Similar to the CloudSat radar-lidar products, DARDAR merges coincident lidar attenuated backscatter measurements obtained from CALIPSO (Cloud, Aerosol Lidar and the Infrared Pathfinder Satellite Observations, Winker et al., 2010) in synergy. Combining these two active instruments, DARDAR is sensitive to both optically thin cirrus in TTL and optically thick deep convective clouds (DCC). It provides the to CPR footprints. Based on an optimal estimation method (Rodgers, 2000), DARDAR iteratively retrieves the state vector which contains visible extinction, lidar extinction-to-backscatter ratio, and particle number concentration and converts it to ice water content (IWC), the effective radius of ice particles, and the visible optical depth of ice clouds, at each CloudSat footprint spaced every 1.1 km.

In this study, we obtain the and effective radii profiles at each CPR footprint with horizontal (cross-track) resolution of 1.4 km and a vertical resolution of 60 m following a set of cloud microphysical parameterizations (i.e., particle size distribution and mass-size relation). This study uses IWC profiles from DARDAR but cloud type classified by the DARDAR-Cloud product

(v2.1.0) and the cloud types from the CloudSat 2B-CLDCLASS-LIDAR product. ~~Discrepancies exist between the CloudSat 2B-CLDCLASS-LIDAR and DARDAR~~ Due to differences in retrieval algorithms and cloud microphysical assumptions (Deng et al., 2013), there are discrepancies between the two products in terms of ice cloud ~~existence. To overcome the discrepancies, a~~ occurrence (McErlich et al., 2021). For consistency, we only use footprints where both radar and lidar observations are available and treat a high cloud layer detected by DARDAR but not classified in 2B-CLDCLASS-LIDAR ~~is treated~~ as the same cloud type as its adjacent cloud layer, or ~~cirrus, as cirrus~~ if it is isolated.

The Aura Microwave Limb Sounder (MLS, Waters et al., 2006) retrieves ~~water vapor above temperature and trace gases~~ for pressure levels less than 316 hPa, with a vertical resolution of around 3 km ~~for water vapor and 4.7 km for temperature~~. The documented accuracy of the version 4.2 product at the level of 100 hPa is 8% for water vapor ~~and 0.7 K for temperature~~. Although MLS can retrieve atmospheric states in moderately cloudy conditions, line shape distortion caused by the strong scattering of thick clouds limits the retrieval capability (Livesey et al., 2017). Therefore, only data not affected by clouds, based on a ~~the~~ status flag ~~of included with~~ the product, are used to avoid degraded data quality. Moreover, due to the limb-viewing scanning geometry, MLS has a relatively large sampling footprint with a horizontal resolution around 200 km along the track, which limits its sensitivity to ~~the~~ small-scale variability (Schwartz et al., 2013).

AIRS measures infrared spectra from 650 cm^{-1} to 2665 cm^{-1} with 2378 channels, using cross-track scans to provide a large spatial coverage ~~of the measurements~~. Only the ~~field-of-views~~ fields-of-view (FOVs) with viewing angles within ~~15° from the nadir are used~~ 15° of the nadir is used in this study, considering that the limb-view geometry increases the optical depth and the atmospheric attenuation. The selected viewing angle corresponds to a cross-track span of around 400 km. The high spectral resolution in the mid-infrared makes it ~~AIRS~~ sensitive to temperature, water vapor, and also ~~the~~ cloud clouds. However, the standard AIRS retrieval is not sensitive to the water vapor signal from the ~~extremely dry UTLS region (Fetzer et al., 2008; Gettelman et al., 2004; Read et al., 2007)~~. Moreover, the UTLS (Fetzer et al., 2008; Gettelman et al., 2004; Read et al., 2007) ~~because of the weak absorption/emission of the dry UTLS relative to the troposphere and a~~ cloud-clearing ~~retrieval method~~ algorithm (Susskind et al., 2003) adopted by the AIRS standard retrieval. This algorithm infers temperature and trace gases of the clear-sky portion of adjacent 3×3 FOVs with varying cloud amounts by contrasting the nine FOVs, assuming a uniform distribution of these atmospheric states. Consequently, it degrades the horizontal resolution by a factor of three and suffers from large uncertainties ~~in the overcast condition when cloud amounts are uniform or when temperature and trace gases change drastically among the nine FOVs~~.

Therefore, instead of using the AIRS Level 2 product for above-cloud atmospheric conditions, we apply a synergistic, cloudy-sky retrieval method developed from the cloud-assisted method proposed by Feng and Huang (2018). ~~This retrieval method jointly uses~~ Targeting at dense high-level clouds, this retrieval method retrieves water vapor, temperature, ice water content, and effective radius from the AIRS L1B ~~v5 radiance measurements to retrieve water vapor and temperature above dense high-level clouds in FOVs where collocated~~ product by combining active observations of mass concentration and effective size of ice cloud particles from the DARDAR-Cloud ~~contains thick upper-tropospheric clouds. It is hereinafter~~ product. This approach is hereinafter referred to as either a joint AIRS-DARDAR retrieval or a synergistic retrieval. ~~This method is validated in Feng et al. (2021) and is found to be sensitive to the~~ While the information on temperature and water

vapor profiles above clouds is obtained from spectrally-dependent optical depths, the inclusion of active cloud observations substantially reduces uncertainties in cloud top position and hence increases the sensitivity of the retrieval to the temperature and water vapor of topmost cloud layers. Using the wavenumber-dependent cloud extinction coefficients in the mid-infrared channels, this method marginally updates the concentration and effective particle size of ice clouds relative to the collocated cloud observations of active sensors. The effective radius is estimated as a vertically averaged value that produces the most reasonable mid-infrared emission spectra of thick high-level clouds (Feng et al., 2021). Through a simulation experiment, Feng et al. (2021) demonstrated that the synergistic method is sensitive to spatial variability in thermodynamic conditions above deep convections through a simulation experiment. The details convection. Details of this retrieval method are presented in Appendix A. The retrieval achieves a precision of 0.31 K and 0.36 ppmv for temperature and water vapor, respectively, as illustrated by Fig. A2. The vertical resolution at 100 hPa is 3.2 km for temperature and 5.8 km for water vapor.

The impact of cyclones is assessed by ~~the anomalies in clouds~~ calculating anomalies in cloud and non-cloud variables compared to their ~~climatologie~~ climatological values. In this paper, we define the climatology as the multi-year monthly mean of variables from 2006 to 2016, using ~~the IWC from DARDAR v2.1.1~~, temperature from AIRS ~~I2-L2~~ v6, water vapor from MLS v4.2, ~~the brightness temperature and brightness temperatures at 690 and 1231 cm⁻¹ derived from AIRS L1B v5, and the IWC from DARDAR on a 1° × 1°~~. All variables are assessed on a 1° × 1° longitude-latitude grid, unless specified otherwise.

2.2 Compositing method

In this study, a list of tropical cyclones ~~overpassed~~ observed by the A-Train satellites is obtained from the CloudSat tropical cyclone product (2D-TC, Tourville et al., 2015). This product uses best-track information provided from the Automated Tropical Cyclone Forecasting System (Tourville et al., 2015; Sampson and Schrader, 2000) to identify the cyclone center position. Note that only daytime measurements are available after April 17th, 2011, due to a spacecraft battery issue. In addition to CloudSat, we combine CALIPSO, MLS, and AIRS together to provide the cloud ~~distribution~~ distributions and atmospheric states associated with each cyclone overpass.

Measurements are composited ~~with respect relative~~ to cyclone center locations ~~on in~~ the northern part of the West-Pacific region (the boxed region in Fig. 1 (a)) ~~for, given~~ the abundance of data samples in this region. The density of measurement locations ~~of for~~ each instrument is shown in Fig. 1. ~~The samples of~~ Samples from AIRS (Fig. 1 (d)) are of higher density compared to CloudSat (Fig. 1 (b)) and MLS (Fig. 1 (c)) owing to the advantage of the cross-track scanning of AIRS. Considering ~~that the the differences in the~~ sample densities and ~~the~~ FOV sizes of the original measurements of these instruments ~~are~~ different, the cyclone-centered composites are constructed by averaging variables over different spatial scales: 60 km (CloudSat ~~and DARDAR, as well as DARDAR which reports at CloudSat footprints~~), 120 km (MLS), and 20 km (AIRS), to ensure sufficient samples are obtained. Only ~~oceanic observations~~ observations collected over the ocean are used to avoid sample discrepancies arising from land-sea contrast. ~~Fewer~~ While both daytime and nighttime measurements are used, fewer nighttime measurements are available because of the daylight-only operation of CloudSat after 2011.

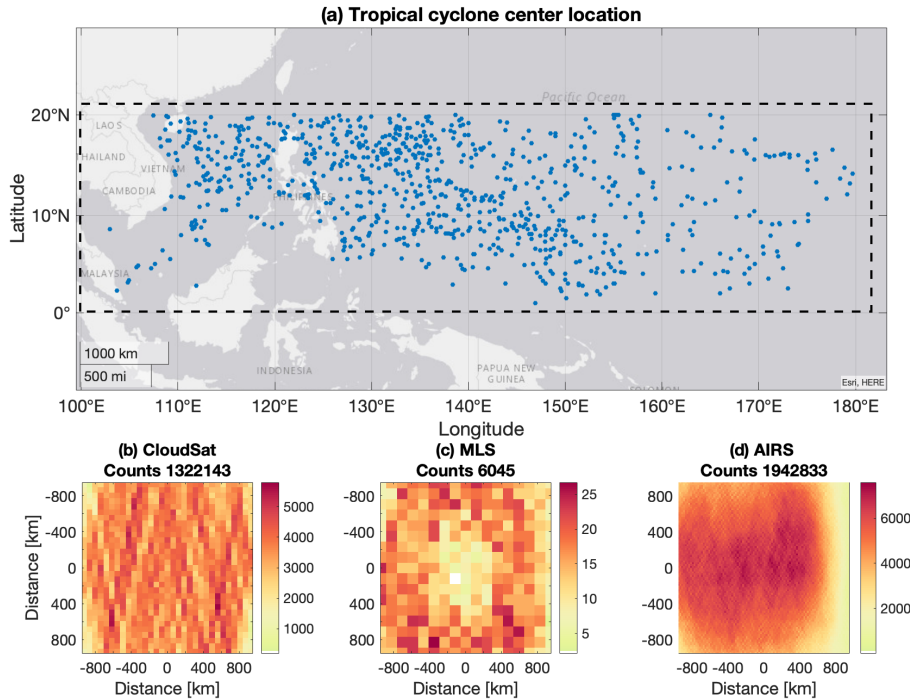


Figure 1. Distributions of cyclone centers ~~overpassed~~ passed over by A-Train and sample density ~~of from~~ of from A-Train instruments with respect to cyclone center locations. (a) ~~Center locations~~ Locations of tropical cyclones ~~centers~~ (947 in total) ~~overpassed that passed over~~ passed over by the A-Train satellites ~~from 2006 to 2016~~ from 2006 to 2016 over the northern part of the West-Pacific region (within the boxed area) ~~from 2006 to 2016~~. The ~~measurement~~ measurement sample density of (b) CloudSat (~~the DARDAR product is available at the horizontal footprints of CloudSat~~), (c) MLS, and (d) AIRS (limited to viewing angles within ~~15° from the 15° of nadir~~ with respect to distances to cyclone center locations). The sample densities are ~~measured~~ measured ~~defined~~ defined as the number of samples per 100 km×100 km ~~and shown at a resolution of area, measured by normalizing sample counts within every 60 km~~ and shown at a resolution of area, measured by normalizing sample counts within every 60 km (b), 120 km (c), and 20 km ~~respectively, for~~ respectively, for (d) ~~grid box over the three instruments~~ grid box over the three instruments area of the grid box. The numbers on the top of each panel show the total number of samples.

195 3 Tropical cyclone impacts

3.1 Cloud distribution

The datasets introduced earlier are used to depict the cloud distributions above cyclones. DCCs and TTL clouds are especially of interest here. ~~DCCs are classified in the CloudSat 2B-CLDCLASS-LIDAR dataset based on several conditions, including a vast horizontal and vertical extent, dense hydrometers, as inferred from radar reflectivity near the cloud top, and also the presence of precipitation (?).~~ TTL clouds, for the convenience of the analysis, are defined as clouds cloud columns with one or more cloud layers above 16 km, where the clear-sky LZRH and the mean tropopause (WMO, 1957) height typically locates in the tropics (Yang et al., 2010). These TTL clouds are further broken into four categories to distinguish TTL clouds with

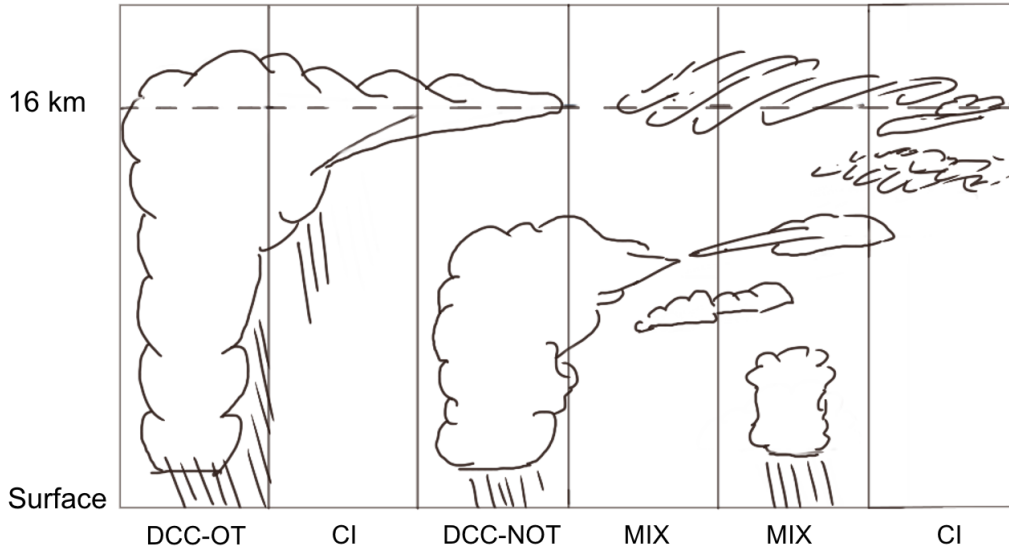


Figure 2. A schematic of the TTL cloud categories (see definitions in Section 3.1).

or without underlying deep convective clouds. As shown by the schematic in Fig. 2, the four cloud categories are defined as follows:

- 205
- DCC-OT: deep convective clouds whose top boundary exceeds 16 km.
 - DCC-NOT: deep convective clouds whose top boundary is below 16 km while non-convective clouds are detected above 16 km.
 - CI: cirrus detected above 16 km and no DCC or any other cloud in the column.
 - MIX: the remaining conditions (no DCC, but cloud detected above 16 km).

210 The DCC-OT category is used to identify continuous convective clouds that extend above 16 km, which is the average altitude of the 380 K isentropic surfaces in the region of interest. These clouds are referred to as “overshooting” DCCs in the context of this paper. For convenience, TTL cloud categories without overshooting, including DCC-NOT, CI, and MIX, are also grouped as TTL-OTHER. Clouds with their top boundary below 16 km are referred to as NTTL.

215 As depicted by Fig. 2, cloud columns with DCCs are classified as either DCC-OT or DCC-NOT, where the former refers to overshooting DCCs and the other refers to any other cloud types that contain DCCs in the column. The two categories are

distinguished by whether the lowermost TTL clouds are connected with underlying DCCs because the adjacent clouds are essentially considered as the same cloud type in the CloudSat-2B-CLDCLASS-LIDAR product. DCC-NOT typically consists DCCs and cirrus with possible middle cloud layers between DCCs and cirrus. In the MIX category, TTL clouds may lie over either middle clouds (accounting for 90% of the MIX category) or low clouds (10% of the MIX category). Columns with only cirrus clouds are classified as CI. MIX and CI categories also include optically thick anvil clouds near the edge of DCCs, because anvil cloud is classified as cirrus or altostratus in the 2B-CLDCLASS-LIDAR (Wang et al., 2012; Young et al., 2013) depending on its vertical position.

The occurrence frequency of clouds and four cloud categories is then calculated as the ratio between the number of samples with a certain feature, e.g., TTL clouds, and the number of overpass samples in each $60 \text{ km} \times 60 \text{ km}$ grid box in the cyclone-centered composite domain (Fig. 3 (a-b,d-g)). Using IWC profiles from the DARDAR-Cloud, a composite of ice water path (IWP) is derived in the same grid boxes. These results are also shown as a function of radial distance to/from the cyclone center in Fig. 4 (a-c).

~~Fig-~~

Figures 3 (a) and Fig. 4 (a) show that TTL clouds occur frequently above tropical cyclones. In the $2000 \text{ km} \times 2000 \text{ km}$ cyclone-centered composite domain, TTL clouds have an occurrence frequency of 0.37 on average, which is significantly greater than the climatology-climatological value of 0.03. This climatology-climatological value is derived from the DARDAR-Cloud from 2006 to 2016, regardless of the presence of cyclones. DCCs occur mostly within 400 km from/of the cyclone center (Fig. 4 (a)) and are noticeably more often on the southwest side of the tropical cyclones (Fig. 3 (b)). The occurrence frequency of DCCs in the composite domain is 0.1 on average, while the climatology-climatological value (regardless of cyclone condition) is only 0.008. These results suggest that tropical cyclones considerably increase the occurrences-occurrence frequencies of both DCCs and TTL clouds.

Figures 3 (d-g) and 4 (b) break down the occurrence frequencies of different TTL cloud categories. They show that DCC-OT tends to occur in the southwest quadrant within the 400 km radius. Outside the quadrant, the CI category has an occurrence frequency generally over 0.2 which makes up over 60% of the total TTL cloud occurrence. It suggests that the formation of high clouds are greatly promoted by tropical cyclone events, possibly by 1) transport of cloud ice via convective outflow from cyclone centers and propagating waves and 2) by local cooling that condensates supersaturated water vapor into ice (Tseng and Fu, 2017; Schoeberl et al., 2019) as a result of dynamical and radiative cooling which is discussed in Sections 3.3.1 and 4.

In contrast to the uniformly distributed TTL cloud (Fig. 3 (a)), Fig. 3 (c) shows that the TTL cloud ice is concentrated in regions closest (within 200 km) to the cyclone center, preferably-most often to the southwest, similar to the DCCs-DCC-OTs (Fig. 3 (bd)). This coincidence suggests a linkage between TTL cloud ice and potential contributions from DCCs that penetrate the bottom of TTL (the 16 km altitude). We refer to them as the “overshooting” DCCs in the context of this paper.

TTL clouds then are broken into four categories to distinguish TTL clouds with or without underlying deep convections. As shown by the schematic in Fig. 2, the four cloud categories are defined as follows:-

– DCC-OT: overshooting DCCs, whose top boundary exceeds 16 km-

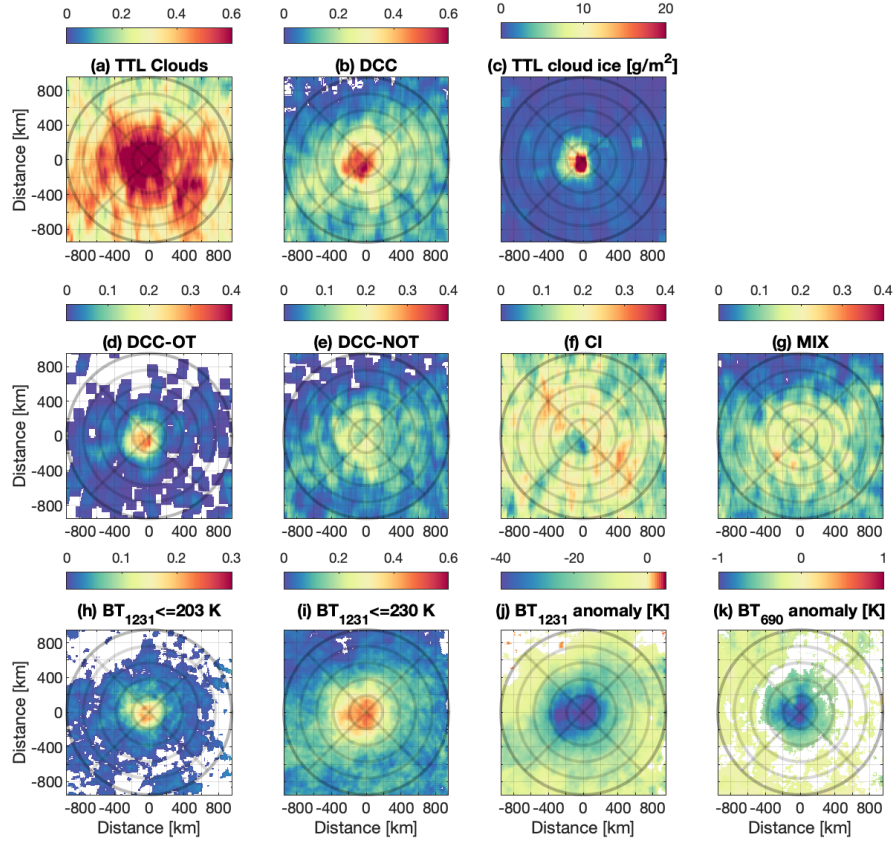


Figure 3. Cyclone-centered composite of cloud statistics. (a) The occurrence frequency of TTL clouds (i.e., clouds above 16 km) and (b) deep convective clouds (regardless of TTL cloud occurrence). (c) Ice water path (g/m^2) above 16 km. The occurrence frequency of four TTL cloud categories (defined in Section 3.1 and schematically shown in Fig. 2): (d) DCC-OT (overshooting DCCs), (e) DCC-NOT (non-overshooting DCCs), (f) CI (cirrus), and (g) MIX (remaining conditions). The occurrence frequency of clouds identified by infrared radiance measurements: (h) deep convective clouds with $BT_{1231} \leq 203$ K and (i) overcast high clouds with $BT_{1231} \leq 230$ K. (j) Brightness temperature anomalies [K] in an atmospheric window channel (BT_{1231}) and (k) a CO_2 channel (BT_{690}). Upper (a-c), middle (d-g), and lower (h-k) panels are based on data from DARDAR-Cloud-IWC, CloudSat-2B-CLDCLASS-LIDAR, and the AIRS L1B v5 product, respectively. Only statistically significant occurrence frequencies (at a 99% confidence level, compared to zero) are shown in (a,b,d-i), and only significant brightness temperature anomalies (99%, compared to the climatology) are shown in (j,k).

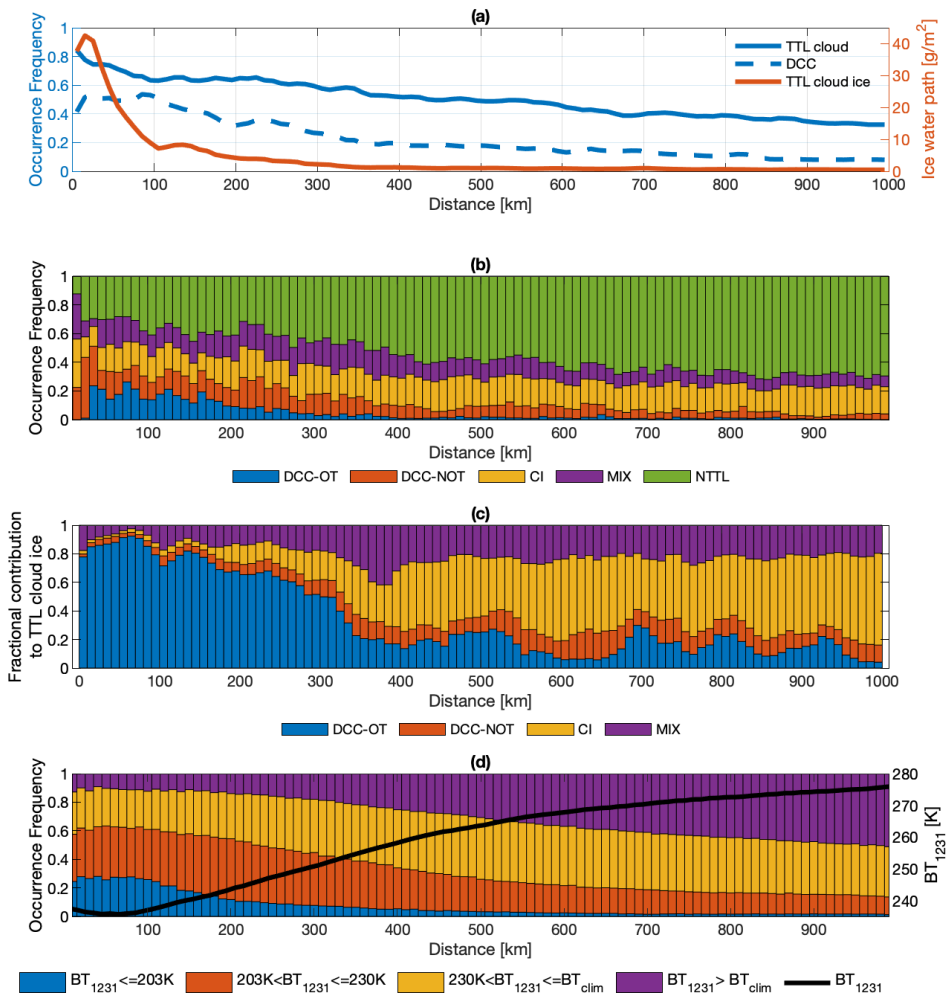


Figure 4. Cloud statistics as a function of radial distance to cyclone center. (a) Occurrence frequency of TTL clouds (blue solid curve) and deep convective clouds (blue dashed curve); the red curve is the ice water path (g/m^2) above 16 km. (b) Occurrence frequency of each cloud category (schematically shown in Fig. 2). (c) Fractional contribution to the TTL cloud ice (the red curve in panel (a)) by each cloud category. (d) Occurrence frequencies of clouds classified by BT_{1231} . BT_{clim} refers to the multi-year monthly mean BT_{1231} . The black curve shows the average BT_{1231} .

- DCC-NOT: non-overshooting DCCs, whose top boundary is below 16 km, while cloud detected above 16 km.
- CI: cirrus detected above 16 km and no DCC or any other cloud in the column.
- MIX: the remaining conditions (no DCC, but cloud detected above 16 km).

255 Cyclone-centered composite of cloud statistics: (a) The occurrence frequency of TTL clouds (i.e., clouds above 16 km) and (b) deep convective clouds (regardless of TTL cloud occurrences). (c) Ice water path (g/m^2) above 16 km. The occurrence frequency of four cloud categories (schematically shown in Figure 2): (d) DCC-OT, (e) DCC-NOT, (f) CI, and (g) MIX. The occurrence frequency of clouds identified by infrared radiance measurements: (h) deep convective clouds with $BT_{1231} \leq 203$ K and (i) overcast high cloud with $BT_{1231} \leq 230$ K. (j) Brightness temperature anomaly K in atmospheric window channel (BT_{1231}) and (k) CO_2 channel (BT_{690}). Upper (a-e), middle (d-g), and lower (h-k) panels are based on data from DARDAR cloud-IWC, CloudSat-2B-CLDCLASS-LIDAR, and AIRS-L1B product, respectively. Only statistically significant occurrences (at a 99% confidence level, compared to zero) are shown in (a,b,d-i), and only significant brightness temperature anomalies (99%, compared to the climatology) are shown in (j,k).

265 Cloud statistics as a function of radial distances to cyclone center. (a) Occurrence frequency of TTL clouds (blue solid curve) and deep convective clouds (blue dashed curve); the red curve is the ice water path (g/m^2) above 16 km. (b) Occurrence frequency of each cloud category (schematically shown in Figure 2). (c) Fractional contribution to the TTL cloud ice (the red curve in panel (a)) by each cloud category. (d) Occurrence frequencies of clouds classified by BT_{1231} . BT_{clim} refers to the multi-year monthly mean BT_{1231} . The black curve shows the average BT_{1231} .

A schematic of the TTL cloud categories (see definitions in Section 3.1).

270 For convenience, TTL cloud categories without overshooting, including DCC-NOT, CI, and MIX, are also referred to as TTL-OTHER. Clouds with their top boundary below 16 km are referred to as NTTL.

As depicted by Fig. 2, we distinguish the DCC-OT and DCC-NOT by whether the lowermost TTL clouds are connected with underlying DCCs, because the adjacent clouds are essentially considered as the same cloud type in the CloudSat cloud classification dataset (2B-CLDCLASS-LIDAR). Columns with only cirrus clouds are classified as CI. In the MIX category, the TTL clouds may lie over either middle clouds (accounting for 90% of the MIX category) or low clouds (10% of the MIX category). MIX and CI categories also include optically thick anvil clouds near the edge of DCCs, because anvil cloud is classified as cirrus or altostratus in the 2B-CLDCLASS-LIDAR (Young et al., 2013), depending on its vertical position.

280 Following this classification, we compute the occurrence frequency of each cloud category and their (DCC-OTs) to TTL cloud ice. Hence, we calculate the fractional contribution to TTL cloud ice in a grid box is calculated from each TTL cloud category, defined as the ratio between the sum of TTL cloud ice of one cloud category and the total TTL cloud ice. Figure 4 (c) confirms that DCC-OTs frequently occur within the 400 km radius, accounting for the majority account for over 80% of TTL cloud ice (Fig. 4 (e)). CI category has an occurrence frequency generally over 0.2, which makes up over 60% of the total TTL clouds occurrence outside the 400 km radius (Fig. 3 (f) and Fig. 4 (b)), but contributes little to the TTL cloud ice (Fig. 4 (e)). near the cyclone center. After integrating over the area within 1000 km of cyclone centers, DCC-OT accounts for 43% of the cloud ice with only 5% of the observed TTL cloud over, while

285 CI accounts for 23% of the cloud ice with 48% of the observed TTL cloud cover. Overall, Fig. 3 and 4 ~~depict-suggest~~ that most TTL clouds above cyclones are ~~of the C type~~ cirrus above a clear troposphere (CI), while the TTL cloud ice is ~~dominantly contributed-largely contained~~ by overshooting deep ~~convections (DCC-OT)~~ convective clouds (DCC-OTs).

3.2 Infrared Radiance

In the previous section, the distribution patterns of ~~cloud-clouds~~ above tropical cyclones are analyzed by ~~combing-combining~~ 290 observational products from CloudSat and CALIPSO. Compared with the nadir-view-only instruments, AIRS provides ~~continual expanded~~ spatial coverage by performing a cross-track scan. With over two thousand channels, this hyperspectral instrument ~~sounds-can profile~~ atmospheric absorbers and temperatures ~~at different altitudes~~. For example, the brightness temperature (BT) ~~at-in~~ the atmospheric window channel is ~~sensitive-to-the-cloud-top-temperature-for-inferring-the-a-measure-of-cloud-thermal-emission-temperature-which-is-useful-for-inferring~~ cloud top height.

295 As ~~discovered-described~~ in Section 3.1, ~~overshooting-DCCs-are-the-overshooting~~ DCC is a major source of ~~the-TTL~~ cloud ice. The spectral signatures of the overshooting DCCs are further investigated. Previous studies (Aumann et al., 2011; Aumann and Ruzmaikin, 2013) have shown that overshooting DCCs are identifiable by cold BT anomalies in the window channels, e.g., at the 1231 cm^{-1} channel (BT_{1231}) and also positive BT difference between the water vapor and window channels ($\Delta BT = BT_{1419} - BT_{1231}$), (Aumann et al., 2011; Aumann and Ruzmaikin, 2013). The cold BT_{1231} is a result of ~~the~~ extremely high 300 vertical reach (and thus the very low cloud top temperature) of the DCCs; the positive ΔBT indicates emission from warm stratospheric layers against the cold cloud top. However, there is no consensus on the threshold values of these quantities to identify DCCs, partly because of ~~the-uncertainty~~ in the temperature distribution above ~~the-DCCs~~ due to the ~~impact-impacts~~ of convection. Following the statistical analysis detailed in Appendix B, we find the optimal threshold for identifying overshooting DCCs to be $BT_{1231} \leq 203\text{ K}$, corresponding to a false positive rate of 0.008 and a false negative rate of 0.323. We find that 305 incorporating ΔBT does not improve the detection.

~~We-then-apply-this-This~~ $BT_{1231} \leq 203\text{ K}$ criterion is then applied to AIRS overpass measurements (Fig. 1 (d)). ~~Fig-Figure~~ 3 (h) shows that the identified deep ~~convections-convective clouds~~ by this criterion ~~distribute-are distributed~~ similarly to the overshooting DCC (DCC-OT) classified by CloudSat. It also confirms ~~a-southwest-preference-for-overshooting-DCC-to-occur~~ that overshooting DCCs prefer to occur in the southwest quadrant.

310 Similarly, a $BT_{1231} \leq 230\text{ K}$ criterion is used to identify thick upper-tropospheric clouds. This criterion detects cloud tops above 11 km, which corresponds to a ~~elimatologic-climatological~~ mean temperature of 230 K. The identified upper-tropospheric clouds ~~distribute-are distributed~~ mainly within the 400 km radius, as depicted in Fig. 3 (i), with a frequency of ~~over-more-than~~ 0.3. ~~Fig-Figure~~ 3 (i) also reveals fewer thick high clouds on the ~~northwest-side-northwestern quadrant~~ of the domain, similar to the results based on CloudSat data (Fig. 3 (e,g)). This BT_{1231} criterion is also used for identifying FOVs 315 with thick upper-tropospheric clouds to perform the synergistic retrieval method discussed in Section 3.3.

For each AIRS overpass sample, the BT_{1231} anomaly is calculated as the deviation from the climatology. As shown in Fig. 3 (j), cyclones induce a significant cold anomaly in BT_{1231} over the composite domain.

The reduced window channel radiance (BT_{1231}) suggests that cyclone clouds effectively attenuate the infrared radiation emitted from the surface, thus potentially leading to a net radiative cooling of the atmospheric layers above the clouds. Hence, it is interesting to examine whether tropical cyclones leave detectable signatures in the temperature fields. A composite of BT anomalies using a CO₂ absorption channel (690 cm⁻¹) is shown in Fig. 3 (k). This channel has a weighting function that peaks at 85 hPa, thus being and is thus sensitive to the cold point temperature temperatures (i.e., the minimum temperature) which vertical temperature minima that climatologically occurs near this level. Indeed, Fig. 3 (k) shows a cold BT_{690} anomaly above cyclones, especially around the cyclone center. However, we cannot eliminate the possible impacts of cloud emission, which will be addressed in the following section using different methods, including a synergistic retrieval that we developed using the have developed for application to A-Train data.

3.3 Temperature and water vapor

In the previous sections, we find substantial increases in cloud occurrence and cloud ice above tropical cyclones. While the increase of TTL clouds is direct evidence of cross-tropopause transports, previous Previous studies (Ueyama et al., 2018; Schoeberl et al., 2018) have suggested that the injection of TTL cloud ice can lead to either hydration or dehydration, depending on the pre-existing conditions. Hence, it is important to examine the water vapor field above the tropical cyclones to ascertain the both the sign and the magnitude of the (de)hydration impact.

A joint AIRS-DARDAR retrieval method has been developed to retrieve atmospheric conditions above thick upper-tropospheric clouds, combining hyperspectral infrared radiances from AIRS and collocated IWC profiles from DARDAR-Cloud. The retrieval method was described in detail and validated using a simulation experiment in (Feng et al., 2021). In summary, the retrieval can achieve a precision of 0.31 K and 0.36 ppmv for temperature and water vapor at 100 hPa, respectively. Feng et al. (2021). Additional information is provided in Appendix A to explain how the temperature and water vapor above tropical deep convections convection are retrieved.

The AIRS FOVs selected for the synergistic retrieval are within 6.75 km (half of the AIRS nadir footprint size) to the nearest DARDAR cloud profile and have window band brightness temperature temperatures (BT_{1231}) colder than 230 K. The BT_{1231} threshold ensures that liquid clouds can be neglected in the retrieval. The frequency of AIRS FOVs passing this criterion is shown in Figure Fig. 3 (i) and Figure Fig. 4 (d). The selection of FOVs is illustrated in Figure Fig. 6 for a tropical cyclone event. In this figure, the brightness temperature in a window channel from AIRS L1B observation depicts a typical cyclonic cloud distribution. The vertical cross-section illustrates the retrieval over selected AIRS FOVs. The same data selection and retrieval processes are performed for all tropical cyclone overpasses. In total, 3475 FOVs from 345 tropical cyclone events are selected and among them, with 2735 profiles are successfully retrieved (reaching convergence in the iterative retrieval procedure). The converged retrievals mostly locate are mostly located within 500 km from of the cyclone center; their distributions are shown in Figure Fig. 5 (b). The constructed cyclone-centered composites of 740 FOVs do not converge and are not used for further analysis. These FOVs typically have large radiance residuals between AIRS observations and the forward model calculations using cloud states from DARDAR-Cloud and prior atmospheric states as inputs. Possible causes of non-convergences include 1) non-uniform cloud cover among the FOVs so that the 1.4 km × 1.8 km CloudSat footprints

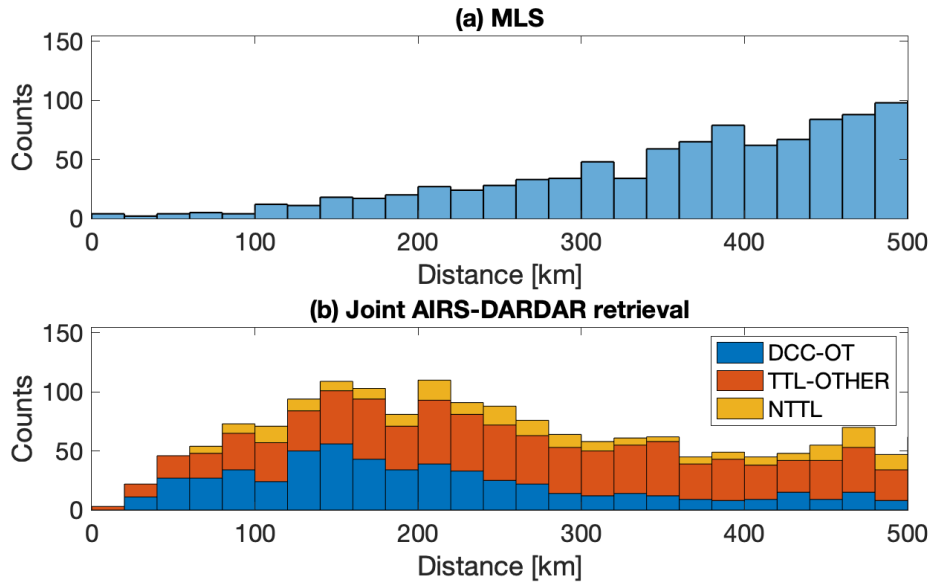


Figure 5. ~~Sample-Sample~~ densities used for assessing temperature and humidity distributions from (a) MLS and (b) ~~the~~ joint AIRS-DARDAR retrieval.

~~are not representative of the $13.5 \text{ km} \times 13.5 \text{ km}$ AIRS FOVs, and 2) the optical thickness of the topmost cloud layer is smaller than one so that the assumption of vertically uniform optical properties per cloud mass does not hold in the radiative transfer calculations (Feng et al., 2021). The retrieved temperature, water vapor, and ~~cloud~~clouds, are shown as a function of vertical~~

355 level and radial distance in Fig. 7 (a,e).

Owing to smaller horizontal sampling footprints and the availability of collocated cloud observations, the synergistic retrieval can reveal ~~the-relatively~~ small-scale variations in the thermodynamic fields above TTL clouds. ~~In-order-to-To~~ understand whether overshooting ~~convections-have-convexion-has~~ a direct impact on water vapor, retrieved samples are classified into overshooting DCCs (DCC-OT) ~~and~~, non-overshooting TTL clouds (TTL-OTHER), and non-TTL clouds (NTTL), using the

360 same cloud classification introduced in Section 3.1 ~~and Fig. 2~~. The converged profiles contain 731 DCC-OTs, 1508 TTL-OTHERs, and 496 NTTLs; ~~their sample densities-the sample counts~~ are shown in ~~Figure-Fig.~~ 5 (b). The mean profiles for each category are shown in ~~Figure-Fig.~~ 9 (a,b). ~~These samples are representative of the cloud categories but may not be representative of the geographical distributions because the number of samples within each radius bin is limited.~~

Meanwhile, similar cyclone-centered composites of thermodynamic fields are constructed using MLS v4.2 and ERA5 (Hers-

365 bach et al., 2020) in Fig. 7. The sample locations of ERA5 are identical to the measurement locations used for the ~~synergistic~~ (joint AIRS-DARDAR) retrieval. The measurement locations of MLS products used in this study are shown in Fig. 1 (c) and Fig. 5 (a). The sample density of MLS near the cyclone center is lower because only measurements not affected by high clouds are used. Figure 7 also shows composites of IWC ~~from~~ from the synergistic retrieval (Fig. 7 (a,e)), ~~from~~ DARDAR-Cloud (Fig. 7 (b,f)) ~~from~~ corresponding to measurements shown in Fig. 1 (b)), and ~~from~~ ERA5 (Fig. 7 (c,g)) at retrieved sample locations;

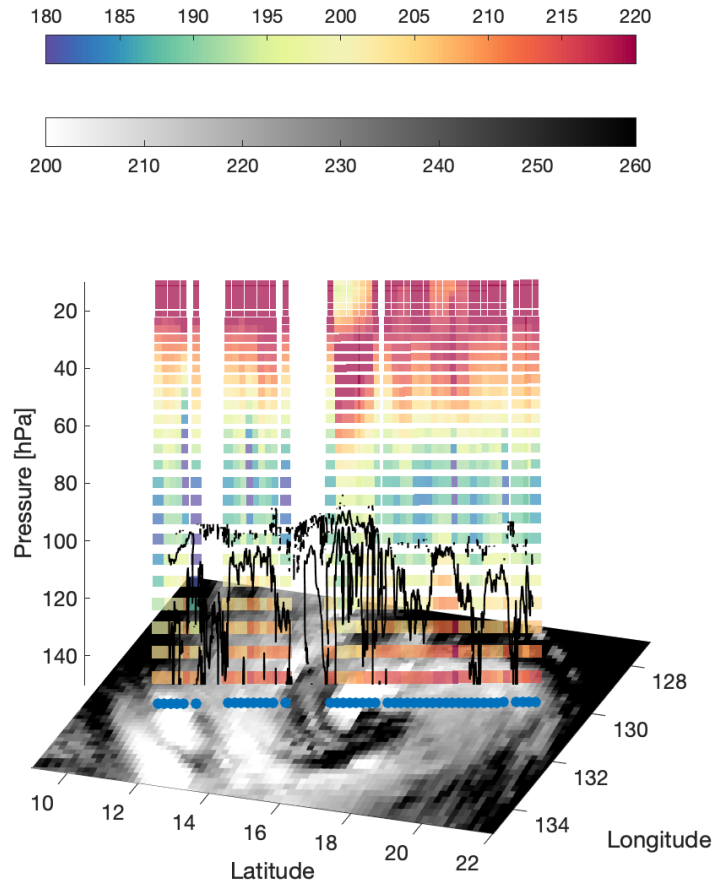


Figure 6. A-Train overpass and retrieval-in-retrievals of a tropical cyclone event on October 2nd, 2007. The underlying image in greyscale shows the brightness temperature at-in a window channel (BT_{1231} ; [K]) from the AIRS L1B v5 product and indicates the cloud-top temperature. The vertical cross-section in color contour-contours illustrates the temperature ([K]) retrieval over thick upper-tropospheric clouds (BT_{1231} colder than 230 K) using the synergistic method described in the textstext; the black line marks the IWC at 10^{-4} g/m³ based on the DARDAR data and outlines the cloud top positions.

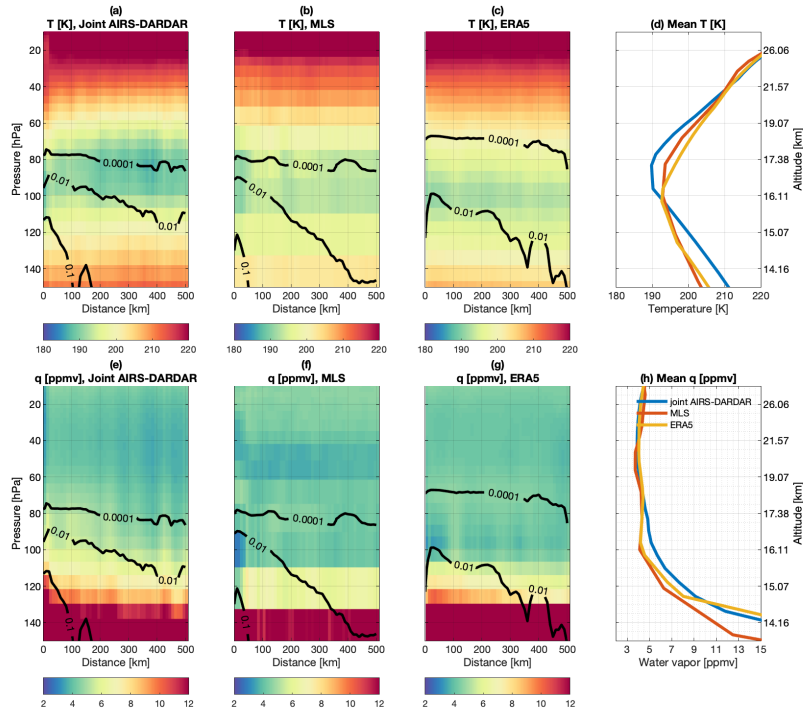


Figure 7. Cyclone-centered composites of temperature [K], water vapor [ppmv], and ice water content [g/m^3]. Temperature (a) and water vapor (e) from the joint AIRS-DARDAR retrieval; the sample counts of samples are shown in Fig. 5 (b). Temperature (b) and water vapor (f) from the MLS v4.2 product; the sample counts of samples are shown in Fig. 1 (c) and Fig. 5 (a). The IWC is from the DARDAR-Cloud; the sample density is shown in Fig. 1 (a). Temperature (c) and water vapor (g) from the ERA5 product sampled at the same locations as (a,e). Mean temperature (d) and water vapor (h) profiles from the different datasets.

370 respectively. We note that there is no collocation between DARDAR-Cloud-CloudSat/CALIPSO (DARDAR) and MLS in Fig. 7 (b,f) as only MLS observations not impacted by high clouds are selected.

The effects of cyclones on temperature and water vapor are examined by subtracting the multi-year monthly mean at every sample location from Figure Fig. 7. The anomalous thermodynamic fields are presented in Figure 8 Fig. 8, while the mean anomalies for the three cloud categories (DCC-OT, TTL-OTHER, and NTTL) are shown in Figure Fig. 9 (c,d). For MLS and 375 ERA5, the monthly mean climatologies are constructed using the same dataset (MLS or ERA5, respectively). For the synergistic retrieval, there is no available ‘climatology’ from this retrieval dataset for non-cyclonic conditions. AIRS L2 temperature and MLS water vapor products are used instead, which are converted to the same vertical resolution to reduce the systematic bias, as described in Appendix A.

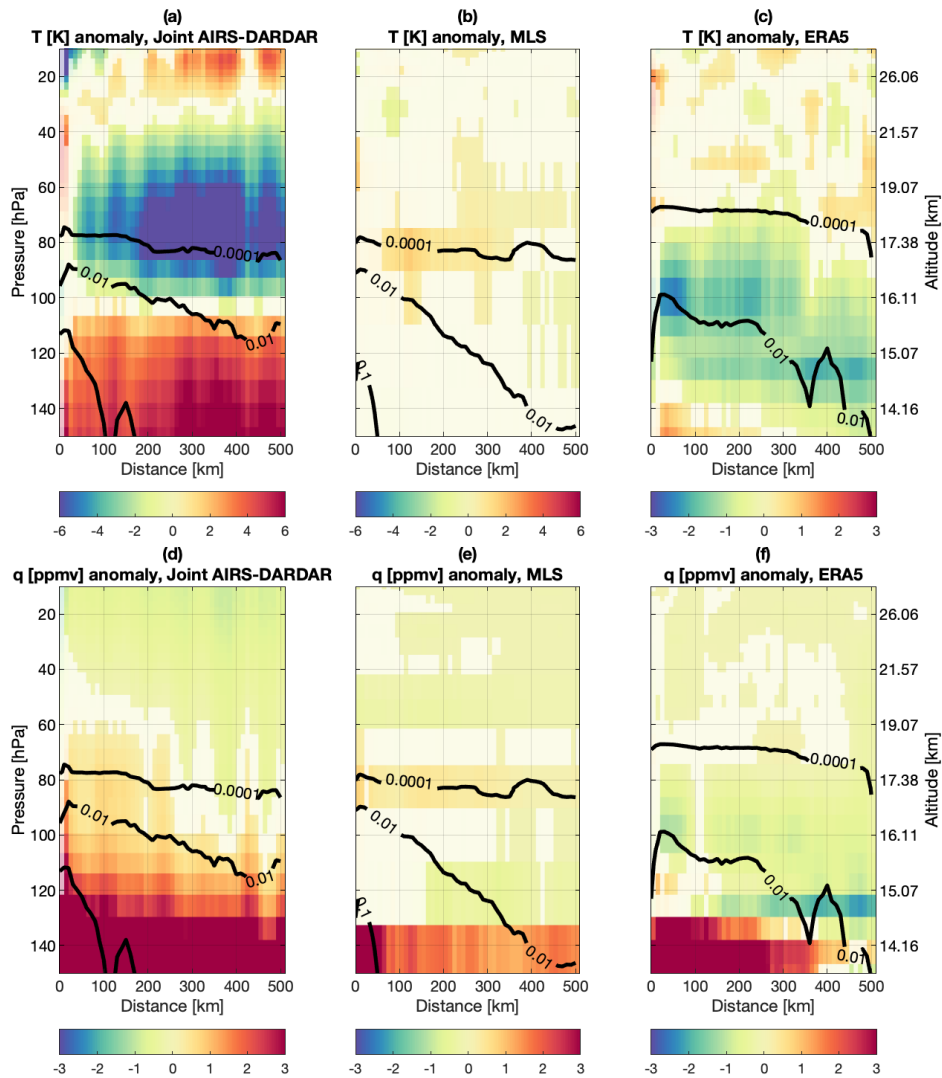


Figure 8. Temperature Cyclone-centered composites of temperature and water vapor anomalies above tropical cyclones. Anomalies below the 99% confidence level are set to be transparent. (a,d) Similar to [Figure Fig. 7](#) (a,e) but after subtracting the climatologies of temperature from the AIRS L2 v6 product and water vapor from the MLS v4.2 product, respectively. (b,e) Similar to [Figure Fig. 7](#) (b,f) but after subtracting the climatologies of temperature and water vapor from the MLS v4.2 product. (c,f) Similar to [Figure Fig. 7](#) (c,g) but after subtracting the climatologies of temperature and water vapor from ERA5.

3.3.1 Temperature

380 Using the synergistic retrieval, we find that tropical cyclone events lead to an oscillating pattern of temperature anomalies above the cloud top (Fig. 8 (a)). This ~~pattern~~ shifts the cold-point tropopause to higher altitudes (see also Fig. 9 (a)). Compared ~~to~~ ~~with~~ the climatology, the mean temperature profile above cyclones shows a noticeable negative anomaly between 40 to 100 hPa and positive anomalies at other vertical ranges. We note that this cold anomaly around 80 hPa also ~~confirms~~ ~~supports~~ the cold signature in BT_{690} displayed in Fig. 3 (k). This ~~vertically-oscillating~~ ~~vertically-oscillating~~ anomaly feature is consistent
385 with previous findings using radiosonde and GPS radio occultation measurements (Holloway and Neelin, 2007; Biondi et al., 2013; Rivoire et al., 2016).

The oscillating pattern of temperature anomalies may ~~be-caused-by~~ ~~arise for~~ a few reasons. The good alignment of the cold anomaly with the cloud top position around the cold point (~ 80 hPa) ~~signifies~~ ~~implicates~~ the impact of cloud radiative effects. This motivates us to ascertain the role of radiation in forming the retrieved temperature pattern. The thick cloud layers may
390 absorb ~~the~~ incoming solar radiation to heat the cloud top while attenuating ~~the~~ emission from the warm surface to cool the atmospheric layers above the cloud. These expected cloud radiative effects agree with the signs of temperature anomalies and will be further examined in Section 5. On the other hand, Rivoire et al. (2020) pointed out that ~~the~~ cloud radiative cooling only partly explains the cooling tendency above ~~tropical~~ cyclones. Other mechanisms at play may include the adiabatic expansion (Holloway and Neelin, 2007) ~~of the~~ ~~in~~ convective overshoots (Robinson and Sherwood, 2006) and the outward ~~branch of the~~
395 ~~branches of~~ secondary circulation (Rivoire et al., 2020; Schubert and McNoldy, 2010).

It is also interesting to find that the temperature anomaly is stronger above non-overshooting clouds (TTL-OTHERs) ~~in~~ ~~comparison with~~ ~~than over~~ DCC-OTs ~~and or~~ NTTLs (Fig. 9 (a,c)). ~~It~~ ~~This finding~~ suggests a potential linkage between the temperature anomaly and the formation of TTL clouds. For example, one plausible explanation is that the cooling of air above cyclones promotes the formation of thicker TTL clouds by ~~depositing the pre-existing water vapor~~ ~~favoring water vapor~~
400 ~~deposition~~ onto ice particles, ~~which are evident in Figure as seen in Fig.~~ 9 (d) and ~~Figure ?? as Fig.~~ 10 and discussed in Section 3.3.2.

We note that the significant temperature anomaly pattern ~~disclosed~~ ~~identified~~ by the synergistic retrieval is not found in either MLS or ERA5. Livesey et al. (2017) have documented that MLS temperature ~~retrieval is~~ ~~retrievals are~~ particularly susceptible to cloud contamination, while Schwartz et al. (2008) note that this issue cannot be effectively screened out by the *status* flag of
405 the MLS ~~v4.2~~ product. Therefore, the MLS temperature product may not be able to observe the pattern of temperature anomaly.

By comparing ERA5 (Fig. 7 (c) and Fig. 8 (c)) to the synergistic retrieval (Fig. 7 (a) and Fig. 8 (a)), we find that ~~although~~ ERA5 produces a higher cloud top (marked by 10^{-4} g/m³ IWC contour) than the DARDAR observation ~~but in general~~ ~~underestimates the~~ ~~it generally underestimates~~ TTL cloud ice. ERA5 also exhibits a cold anomaly but places it ~~in at~~ lower altitudes compared to the synergistic retrieval, which is partly attributable to different radiative heating ~~signatures~~ due to dif-
410 ferences in cloud ice. Previous studies (Wright et al., 2020) have also found large discrepancies in the upper-tropospheric temperature and tropical high clouds among reanalysis products, likely due to convective parameterization (Takahashi et al., 2016; Wright et al., 2020).

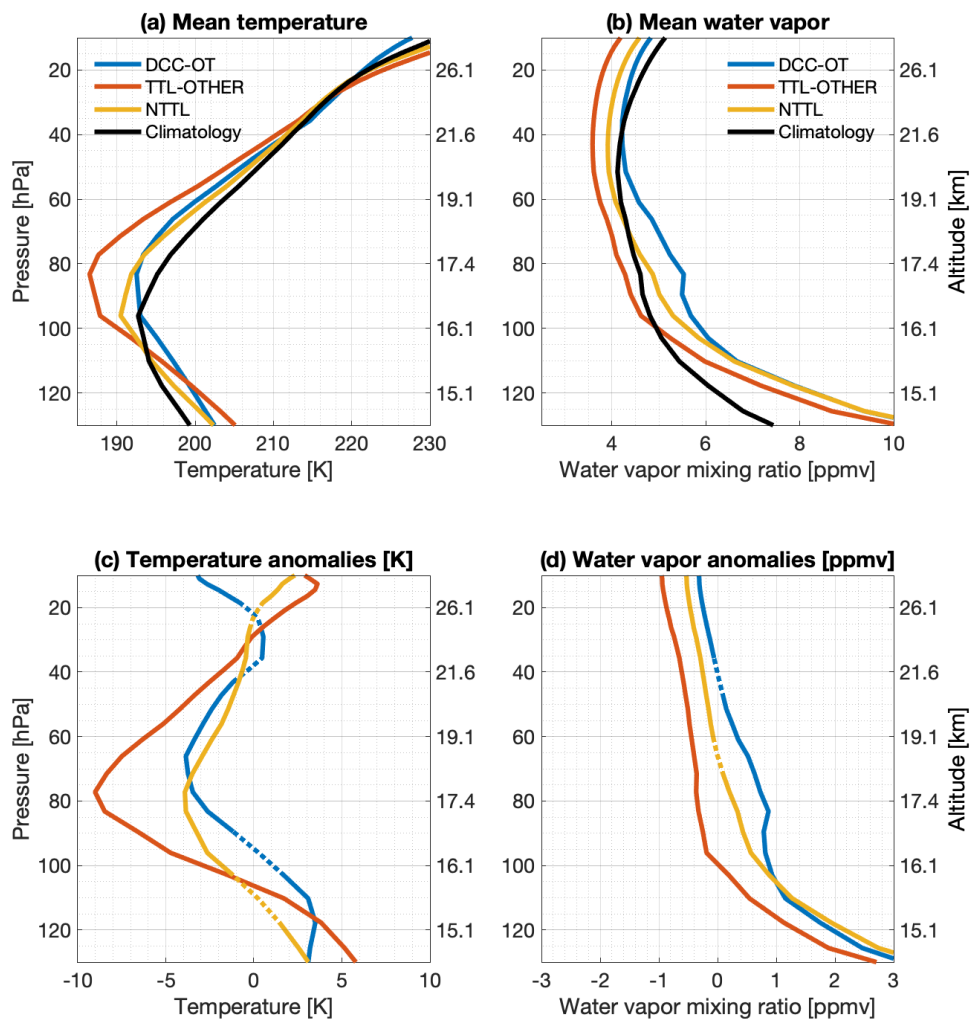


Figure 9. The mean (a) temperature [K] and (b) water vapor [ppmv] profiles above cyclones, for overshooting TTL clouds (DCC-OTs, blue), non-overshooting TTL clouds (TTL-OTHERs, orange) ~~TTL clouds~~, and non-TTL clouds (NTTL, yellow), ~~and along with~~ the climatology (black). (c,d) the same as (a,b), but for anomalies ~~-~~with respect to the climatology.

3.3.2 Water Vapor

Using the synergistic retrieval, Fig. 8 (d) shows that both hydration and dehydration can occur above cyclones. Hydration is
 415 found below 80 hPa, especially near the cyclone center, while dehydration is found above 60 hPa. This finding is consistent

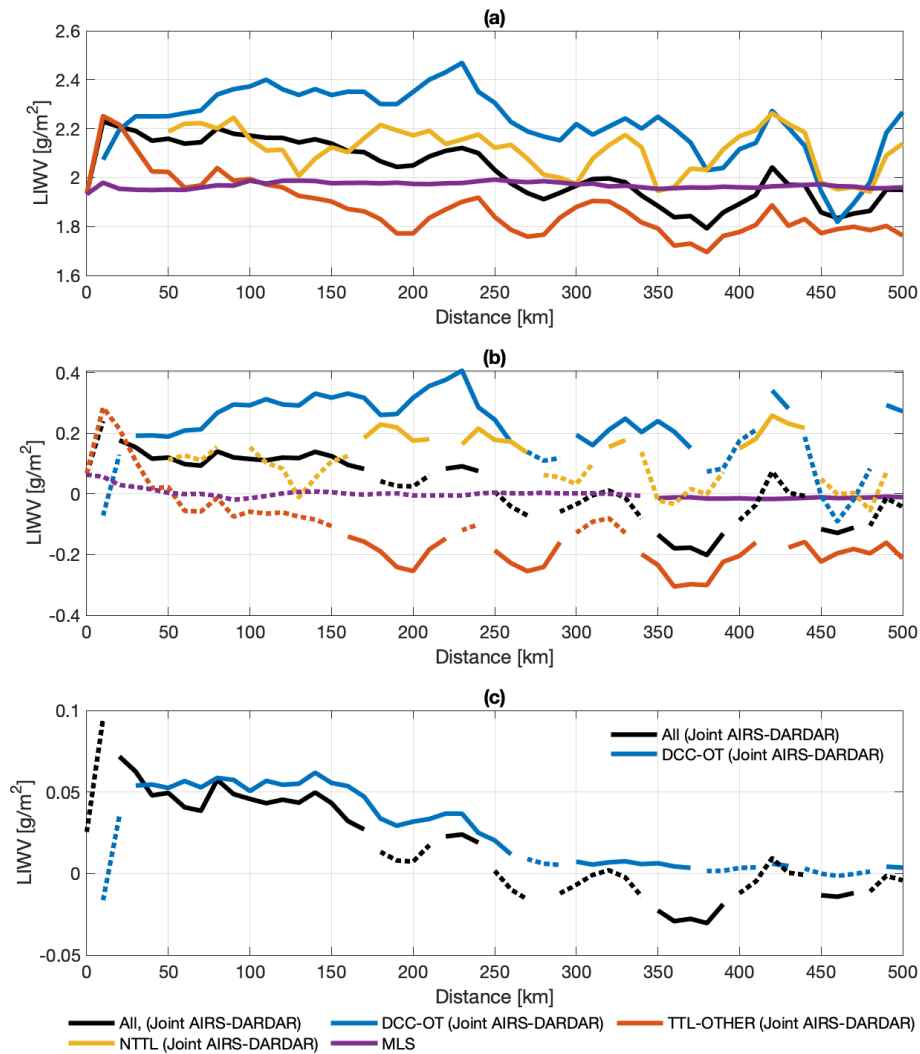


Figure 10. (a) Column-Layer integrated water vapor (CIWV) above 16 km (LIWV) from the joint AIRS-DARDAR retrieval (blueblack) and MLS (blackpurple). Samples retrieved by the synergistic retrieval are separated into overshooting TTL clouds (DCC-OT, redblue) and other non-overshooting TTL clouds (red), and non-TTL clouds (yellow). Solid curves show the statistically significant (99% confidence level) anomaly and anomalies while dashed curves are not statistically significant at the 99% level. (b) Same as (a) except for the anomaly in CIWV-LIWV . (c) Contributions to the CIWV-LIWV anomaly from thick upper-tropospheric clouds ($BT_{1231} < 230$ K, blueblack) and DCC-OTs (redblue).

with MLS ~~observation~~-observations (Fig. 8 (e)), ~~despite that~~ even though the synergistic retrievals are performed above thick upper-tropospheric clouds while the selected MLS observations are high-cloud free.

We note that the synergistic retrieval does not have ~~a high vertical resolution~~ sufficient vertical sensitivity to fully resolve the vertical distribution of water vapor, due to the smearing effect of the averaging kernel discussed in Appendix A. Nevertheless, 420 the retrieval is sensitive to the spatial variability of the ~~column layer~~ integrated water vapor (~~CIWV~~above 16 km (LIWV)), which ~~is validated in Feng et al. (2021) and~~ has been validated by Feng et al. (2021) and in Appendix A. The retrieved ~~CIWV~~LIWV above 16 km is shown in Fig. ~~??-10~~ (a, b) ~~;~~ as a function of radial distance ~~to~~ from the cyclone center. Therefore, we focus on the horizontal variability in ~~CIWV~~of LIWV above cyclones, which can be more confidently detected by the synergistic retrieval, to disclose overall hydration or dehydration above 16 km.

425 The synergistic retrieval detects a decreasing ~~CIWV with the increasing radial distances~~ LIWV with increasing radial distance (Fig. ~~??-10~~ (a,b)). Significant hydration occurs near the cyclone center, increasing the ~~CIWV~~LIWV by up to 0.18 g/m^2 ($\sim 9\%$), while dehydration occurs around a distance of 375 km. In MLS, the ~~CIWV~~LIWV does not substantially differ from the climatology, possibly because MLS samples large, high-cloud free areas.

The (de)hydration impact of cyclones is ~~separated~~ classified after isolating DCC-OTs, TTL-OTHERs, and NTTLs. As depicted in ~~Figure ??~~ Fig. 10 (a,b), significant dehydration is only found above non-overshooting TTL clouds, while significant hydration is found above overshooting clouds and non-TTL clouds. DCC-OTs increase the ~~CIWV~~LIWV above 16 km by up to 0.4 g/m^2 , which is equivalent to 20 % of the climatological value. It suggests that overall the air above cyclones is hydrated by ~~the~~ convection, especially ~~the~~ overshooting convection that ~~penetrated the bottom of~~ penetrates the base of the TTL. The ~~role of~~ non-overshooting TTL clouds (TTL-OTHER), however, ~~is~~ are found to be associated with a ~~drier~~ drier environment, 435 possibly due to the deposition of water vapor onto ice particles in colder temperatures (as ~~evident from Figure~~ suggested by Fig. 8 (a) and ~~Figure~~ Fig. 9 (a,c)).

The occurrence frequency of thick upper-tropospheric clouds (AIRS FOVs being colder than 230 K), above which the synergistic retrieval is conducted, is shown in ~~Figure~~ Fig. 4 (d). The expectation of changes in ~~CIWV~~LIWV contributed by thick upper-tropospheric clouds is then estimated by multiplying the ~~CIWV anomaly~~ (~~Figure ??~~ LIWV anomaly (Fig. 10 (b))) 440 by the occurrence frequency of these clouds (~~Figure~~ Fig. 4 (d), blue and orange areas). ~~Figure ??-10~~ (c) shows that the ~~CIWV~~LIWV above cyclones is expected to be around 0.05 g/m^2 (1.5%) ~~higher~~ larger than the climatology within a 150 km radius of the cyclone center, and to be ~~up to as much as~~ 0.03 g/m² (0.9%) ~~lower~~ smaller at a distance of 375 km. On average, the stratospheric column above thick upper-tropospheric clouds within 500 km ~~from of~~ of cyclone centers is 0.014 g/m^2 moister than the climatology. A similar calculation is performed for DCC-OTs, using the occurrence frequency of DCC-OTs shown by 445 the blue area in ~~Figure~~ Fig. 4 (b). It is found that DCC-OT alone increases the mean ~~CIWV~~LIWV above tropical cyclones by 0.024 g/m^2 , which is around 0.7 % of the ~~climatology~~ climatological value.

In summary, hydration is found to result from overshooting convection, which injects water ~~substance~~ substances directly. The moisture injected by overshoots ~~will hydrate~~ hydrates the surrounding environment so that the cloud-free TTL (NTTLs) also shows higher ~~CIWV~~LIWV compared to the climatology. However, at locations away from overshoots, we find that

450 overflow or pre-existing clouds in the TTL are associated with a colder and drier environment, potentially due to water vapor deposition onto ice particles.

4 Radiative effects

In the context of this paper, we have defined the lower boundary of the TTL to be the clear-sky level of zero-radiative heating (LZRH). ~~The radiative~~ Radiative heating rates in the TTL are crucial, for instance, to the ~~variations of stratospheric~~ cross-tropopause transport of water vapor, as ~~it radiatively drives the air parcel to diabatically ascend to the higher they~~ potentially drive the diabatic ascent of air parcels across isentropic surfaces to the stratosphere. While the ~~previous section~~ has found the overall hydration effect of cyclones ascending motion that prevails in the tropical lower-stratosphere is driven by dissipating waves (Holton et al., 1995; Plumb, 2002), it is found that TTL clouds can heat the air through infrared radiation and is important to explain the mass flux to the stratosphere (Corti et al., 2006; Yang et al., 2010). Hence, we are interested in
460 how ~~the~~ radiative heating rates are perturbed above tropical cyclones and whether this helps retain the moisture ~~in~~ anomaly in the TTL.

Moreover, as indicated by the good-close alignment of cloud boundary and temperature anomalies, ~~the~~ cloud radiative effects may have played a role in forming the temperature anomalies ~~as seen in Figure~~ seen in Fig. 8. Therefore, a cyclone-centered composite of radiative heating rates ~~is constructed~~ using the CloudSat 2B-FLXHR-LIDAR product ~~is constructed~~ to help
465 address these questions.

The cloud radiative effect, measured by the radiative heating rate difference between all-sky and clear-sky overpasses, is shown as a function of pressure level and radial distance ~~to~~ from the cyclone center in Fig. 11 (c,d). Only daytime samples (~~overpassing~~ overpasses at 13:30 local solar time) are used ~~to~~ to exclude the lack of shortwave heating during the nighttime. We identify the LZRH in the heating rate profiles as the level where heating rates change from negative to positive. Note that there
470 is no LZRH identified ~~under in~~ two conditions: in Fig. 11 (a,c) when the longwave heating rate is all-entirely negative in the TTL, and in Fig. 11 (b,d,e) when the net heating rate is all-entirely positive.

In the longwave, Fig. 11 (c) shows that clouds generally heat-produce positive perturbations inside the clouds (below 200 hPa) but cools-strong cooling at the atmosphere near and above the cloud top (marked by the 0.01 g/m³ IWC contour). Fig- Figure 11 (d) shows that this cloud top longwave cooling effect is offset by the shortwave effect. The compensation between
475 longwave and shortwave leads to a net cloud radiative cooling effect in the layers above the cloud top but heating-below-it. It shifts a net cloud radiative heating effect below the cloud top. These effects shift the clear-sky LZRH to higher altitudes, suppressing ~~the diabatic ascents~~ diabatic ascent in the TTL.

The cloud radiative heating composited here, particularly the in-cloud heating (below 0.01 g/m³ IWC contour) and cloud-top cooling feature (above 0.01 g/m³ IWC contour), corroborates the temperature structure retrieved using the synergistic
480 retrieval method (Fig. 8 (a)). It is also consistent with the finding of Rivoire et al. (2020) based on an analysis of COSMIC data, who noted a cooling tendency above 100 hPa that is partially attributable to ~~the radiative effect based on an analysis of the COSMIC data~~ radiative effects.

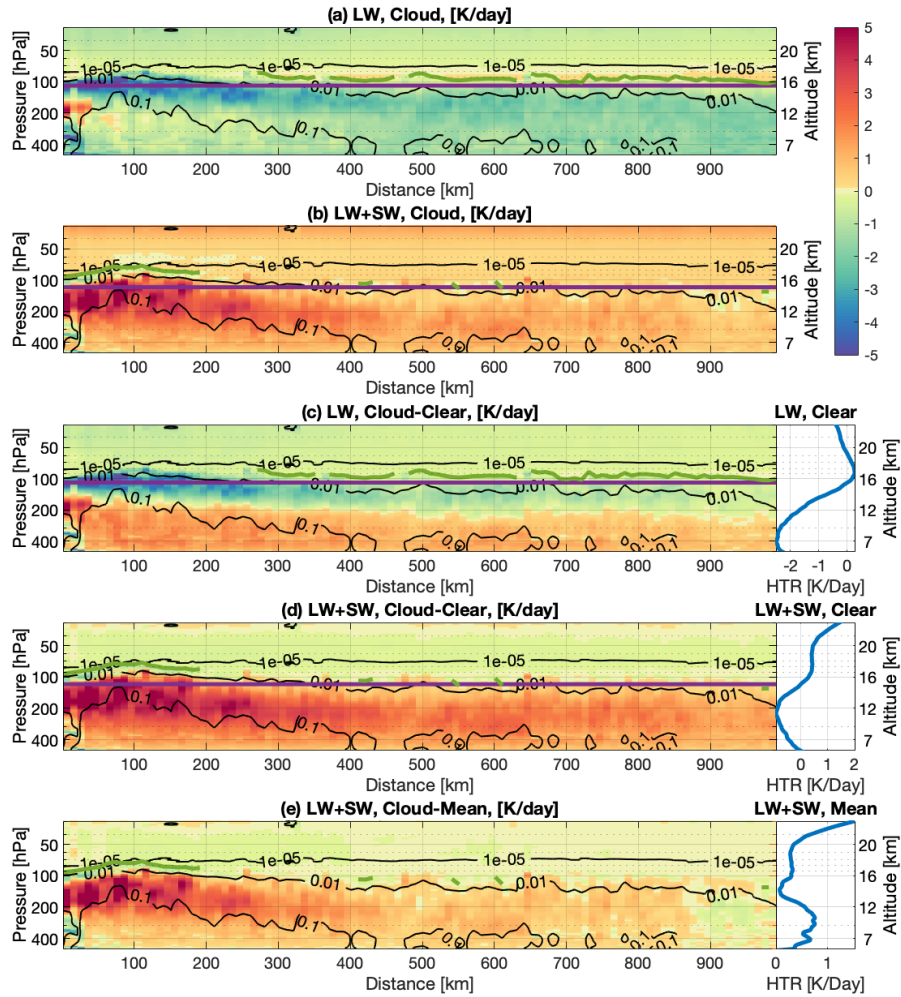


Figure 11. Cloud radiative heating [K/day] as a function of distance to cyclone center. (a) Longwave and (b) net (longwave + shortwave) radiative heating rates from CloudSat [2B-FLXHR-LIDAR](#) product. (c,d) Same as (a,b) but for cloud radiative effects, which are defined as the differences between all-sky heating rates and the mean of clear-sky heating rate (blue curve in the right panel). (e) Same as (d) but for net radiative heating anomalies, which are defined as the differences between all-sky heating rates and the mean all-sky heating rate. Black contour lines show the DARDAR ice water content (g/m^3). The Magenta line marks the clear-sky LZRH. The green line marks the cloudy-sky LZRH, determined as the vertical position where the heating rate changes from positive to negative.

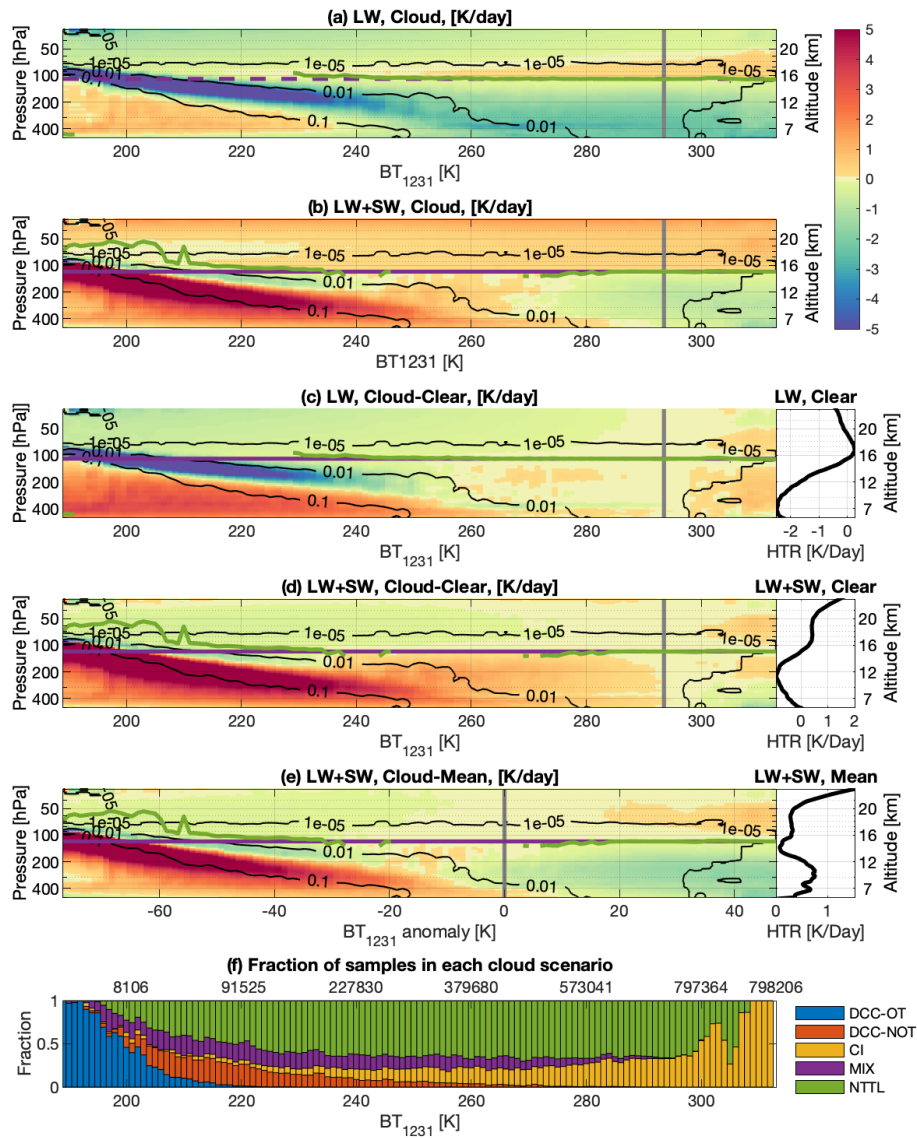


Figure 12. Cloud radiative heating rates [K/day] as a function of window band radiance, BT_{1231} , from collocated AIRS L1B v5 observation. (a) Longwave and (b) net (longwave + shortwave) radiative heating rates from CloudSat 2B FLXHR-LIDAR. (c,d) Same as (a,b) but for cloud radiative effects, which ~~is~~ are defined as the ~~difference~~ differences between all-sky heating rates and the mean ~~of~~ clear-sky heating rate (black curve in the right panel). (e) Net-cloud ~~Same as (d) but for net~~ radiative heating ~~rate~~ rate anomaly ~~difference~~ anomalies, which are defined as the differences between all-sky and the mean ~~of~~ all-sky cyclone overpass (black curve in the right panel). (f) The proportion of samples in each cloud category (classified in Section 3.1) to all cloudy overpass samples. The numbers on the top indicate the number of cloudy samples with BT_{1231} colder than the corresponding temperature marked at the bottom. Black contour lines show the DARDAR ice water content (g/m^3). The Magenta line marks the clear-sky LZRH. The green line marks the cloudy-sky LZRH, determined as the vertical position where the heating rate changes from positive to negative.

Figure Fig. 11 demonstrates that the qualitative structure of cloud radiative heating/cooling changes little with the radial distance. This effects change little with radial distance from the cyclone center. This insensitivity, however, hides the distinct radiative effects of different types of clouds. For instance, it is well known that thin cirrus absorbs longwave DCC cools the atmospheric column above it by trapping the thermal fluxes within the cloud, while thin cirrus can warm the air locally by absorbing the thermal emission from the surface and heats the level it resides (e.g., see Fig. 5 (eb) of Rivoire et al. (2020)); although such an effect is not identified. The compensating sign of radiative effects is not evident anywhere in Fig. 11. Recognizing that clouds types can be differentiated by (c), despite the fact that cloud types have a strong radial dependence (Fig. 4 (b)). Recognizing that the cloud radiative effects are determined by the cloud optical depth and that the window band radiance (BT_{1231}) is sensitive to can be used to characterize the radiative effects of different types of clouds owing to its sensitivity to cloud optical depth over the tropical ocean, we next composite the tropical ocean FOVs.

To construct a composite of cloud radiative heating with respect to BT_{1231} to characterize the radiative effects of different types of clouds.

The CloudSat/DARDAR cloud profile is then, cloud profiles at CloudSat footprints are paired with the nearest AIRS spectra. The AIRS FOVs used evaluated here are limited to those with scanning angles less than 14 degrees, which has a negligible (<3%) effect on optical depth; the distance between CloudSat sampling location and the center of AIRS FOV is within 6.5 km the optical depth and those with CloudSat samples locations fall within their ground footprints (13.5 km). A composite of all-sky radiative heating rates, as well as the differences to clear skies, over every 1-K over every 1-K bin of BT_{1231} , are is shown in Fig. 12, along with differences relative to clear sky conditions.

Fig. 12 discloses shows that different regimes of cloud radiative effects, which we find are well differentiated by BT_{1231} . When BT_{1231} is colder than 230 K (indicating thick upper tropospheric clouds, as discussed in Section 3), net radiative cooling is observed in TTL, the TTL. This net cooling is largely caused by longwave cooling above the cloud tops of DCCs DCC cloud tops (indicated by IWC contours in Fig. 12). Note that this BT condition (colder than 230 K) occurs in more than 50 % of the cyclone overpasses within overpasses within a 300 km radius of the cyclone center (Fig. 4 (d)), indicating that within this radius the TTL is dominated by radiative cooling within this range. In this cloud regime, the cloud effect is to lift lifts the LZRH to higher altitudes, reaching 19.5 km when BT_{1231} is around 200 K. When BT_{1231} is between 240 K and 280 K, noticeable heating emerges near the cloud top emerges (compare Fig. 12 (a) and (b)), attributable to the deeper penetration of solar radiation into the less opaque cloud layer. When BT_{1231} is higher greater than 294 K (the clear-sky climatological mean value), TTL heating is noticed evident. This TTL heating is accompanied by a substantial increase of CIs CI (cirrus) scenes with increasing BT_{1231} as shown in Fig. 12 (f), which suggests the role contribution of thin cirrus in the TTL heating as mentioned above.

Furthermore, we compute the net heating anomaly with respect to the all-sky climatology. The all-sky net heating anomaly is then shown as a function of the BT_{1231} anomaly, which is also defined with respect to the all-sky average, in Fig. 12 (e). It is clear that the cloud effect on the TTL heating rate cloud effects on TTL heating rates above 16 km is are well-differentiated by BT_{1231} : cooling when the BT_{1231} anomaly is negative and heating when the BT_{1231} anomaly is positive. Given that a negative

~~BT₁₂₃₁ anomaly prevails within 1000-km-to-1000 km of the~~ cyclone center (see the black line in Fig. 4 (d)), ~~no-wonder-it-is~~ ~~no wonder that~~ Fig. 11 ~~shows generally~~ ~~generally shows~~ TTL cooling above ~~the~~ ~~tropical~~ cyclones.

The prevalence of ~~radiative-cooling-above-tropical-cyclones~~ ~~TTL radiative cooling in Fig.12 (c,d)~~ suggests that the diabatic
520 ascent that normally (climatologically) occurs within ~~TTL-is-the~~ ~~TTL is greatly~~ suppressed by cloud radiative effects ~~in a~~
~~2000 km × 2000 km domain surrounding tropical cyclone centers~~. A hydrated air parcel above a cyclone has to be advected
further away from ~~eyelone-centers,~~ ~~to-be-radiatively-heated~~ ~~the cyclone centers to experience radiative heating~~ and ascend to
the stratosphere.

~~Lastly~~ ~~Finally~~, it is worth noting a few caveats of the cloud radiative effect assessed here. As the cloud radiative effect
525 is measured by the difference in ~~the~~ radiative heating between ~~all-~~ ~~all-sky~~ and clear-sky conditions, the result is subject to
~~changes-differences~~ in surface emissions and thermodynamic conditions ~~from-between~~ the clear-sky ~~to-and~~ all-sky situations.
We cannot quantify how much ~~TTL-cooling,~~ ~~of the TTL cooling~~ (as shown in Fig. 12 (d,e),-) is directly attributable to clouds ;
because large anomalies in temperature and water vapor ;(as shown in ~~Figure 8,~~ ~~exist-above-the~~ ~~Fig. 8)~~ ~~also exist above tropical~~
cyclones. It is unclear how much these non-cloud variables account for the radiative heating anomalies shown in Fig. 11 and
530 12. Moreover, the CloudSat radiative heating data used here may be subject to errors because their calculation is based on the
ECMWF forecast which does not fully capture the above-cyclone temperature and water vapor ~~variability-perturbations~~ (see
Fig. 8). It is therefore useful to examine the heating rate change above ~~the-these~~ ~~tropical~~ cyclones using collocated observations
of cloud, temperature, and water vapor profiles from our synergistic retrieval.

4.1 Heating rate decomposition

535 Large temperature and water vapor anomalies in the TTL above tropical cyclones (~~as depicted in Fig. 8)~~ are detected using the
joint AIRS-DARDAR retrieval method,~~as depicted in Fig. 8,-~~ Here, using the radiative transfer model RRTM (Iacono et al.,
2000), the radiative effects of the cloud, temperature, and water vapor anomalies are isolated in Fig.~~13,-~~ ~~13~~. The shortwave
effects of temperature and water vapor are not shown because they are negligible compared to the longwave effects.

Following the ~~idea-of~~ Partial Radiative Perturbation ~~approach~~ (Wetherald and Manabe, 1988), we measure the radiative effect
540 of a variable by differencing the RRTM computations with perturbed and unperturbed values of this variable. For instance, the
radiative effect of cyclonic clouds is measured as:

$$dHTR(c) = HTR(c, t_0, q_0) - HTR(c_0, t_0, q_0) \quad (1)$$

Here, ~~HTR-~~ ~~HTR~~ denotes the instantaneous heating rate profile and is computed using RRTM~~-,~~ ~~and~~ ~~c~~, ~~t~~, and ~~q~~ denote
cloud, temperature, and water vapor profiles ;~~respectively,~~ ~~from the cyclone samples,~~ ~~respectively~~. Note that for the ~~t~~ and ~~q~~
545 profiles, only the portions above 16 km are of concern and replaced in the PRP computation. ~~The-variables-~~ ~~Variables~~ with
subscript 0 denote values from the all-sky climatology. The mean ~~of~~ instantaneous longwave and net radiative heating rate
profiles for DCC-OTs, TTL-OTHERs, and NTTLs ;are shown in Fig. 13. The radiative effects of temperature and water vapor
are examined in both all-sky conditions, denoted by the subscript ~~cl~~ ~~d~~ in ~~Figure-Fig.~~ ~~13~~ (g,h), and clear-sky conditions (~~c = 0~~),
denoted by the subscript ~~clr~~ in ~~Figure-Fig.~~ ~~13~~ (c,d).

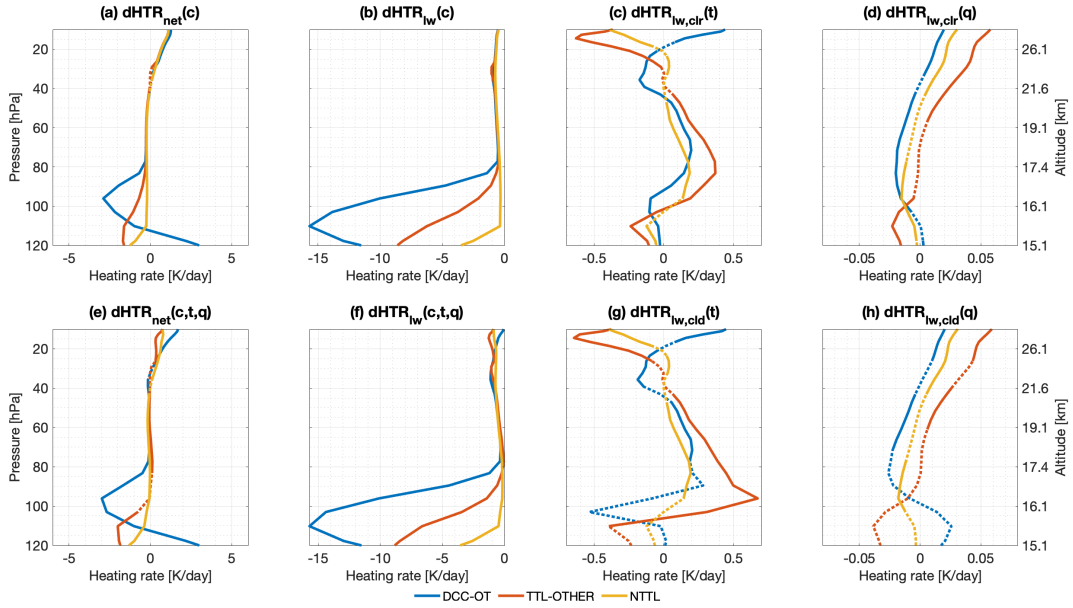


Figure 13. The radiative heating effects of cloud, temperature, and water vapor. (a) The net effects of cloud, $dHTR_{net}(c)$. (b) The longwave effects of cloud, $dHTR_{lw}(c)$. (c) The longwave effects of temperature under for clear-sky conditions, $dHTR_{lw,clr}(t)$. (d) The longwave effects of water vapor under for clear-sky conditions, $dHTR_{lw,clr}(q)$. (e) The net effects of cloud, temperature and water vapor, collectively, $dHTR_{net}(c, t, q)$. (f) The longwave effects of cloud, temperature, and water vapor, collectively, $dHTR_{lw}(c, t, q)$. (g) The longwave effects of temperature under for cloudy-sky conditions, $dHTR_{lw,clد}(t)$. (h) The longwave effects of water vapor under for cloudy-sky conditions, $dHTR_{lw,clد}(q)$.

550 By comparing Fig. 13 (a) and (e), we find that the total net radiative effect, $dHTR_{net}(c, t, q)$, is dominated by clouds. The sign and magnitude of the cloud radiative effect are consistent with our previous conclusion, i.e., namely a cooling effect at the cloud top as indicated by a cold BT_{1231} anomaly (Fig. 12 (a,e)). The cloud longwave cooling effect around 90 hPa is much larger above DCC-OTs due to higher cloud ice water content near this level.

As seen in Fig. 13 (g,h), above 80 hPa where cloud ice diminishes, the all-sky radiative effect of effects of anomalies
 555 in temperature and humidity becomes-become more important. Temperature modulates the longwave emission to modulate
longwave emission in ways that damp the temperature anomalies (compare Fig. 13 (g) to Fig. 9 (c)). For water vapor, a moistening at the cold point increases the thermal emissivity, which leads to cooling at the cold point and heating of at lower levels. Therefore, TTL hydration above DCC-OTs and NTTLs leads to radiative cooling in the TTL. Assuming a similar pattern in thermodynamic anomalies to Figure what is shown in Fig. 9 (c,d) in the clear-sky, we compute the radiative effects
 560 of temperature and water vapor above 80 hPa in the clear-sky (Figure Fig. 13 (c,d)) and find that they are similar to the all-sky results.

Despite the limited vertical resolution of the water vapor retrieval, as discussed in Appendix A, it is ~~of no ambiguity in that~~ the unambiguous that TTL hydration leads to radiative cooling. It suggests that ~~the~~ moisture above overshooting ~~convections~~ convection radiatively cools the layer, thus constraining the moist air from diabatically ascending to higher altitudes. This finding is consistent with the robust radiative cooling seen above cyclones in ~~Figure~~ Fig. 12.

5 Conclusions

In this study, we aim to understand the impacts of tropical cyclones on ~~the~~ thermodynamic conditions in the TTL using multiple instruments aboard the A-Train satellites. We use a TC-overpass product to associate composite multiple observation products ~~for relative to~~ 947 tropical cyclone center locations over the northern part of the West-Pacific region to ascertain the effect of cyclones. To address the lack of reliable observations of temperature and water vapor when thick convective clouds are present, a retrieval scheme proposed by ~~Feng and Huang (2018)~~ Feng and Huang (2018) is improved by incorporating cloud properties measured by active sensors to retrieve the above-cyclone temperature and water vapor ~~profile from infrared hyperspectral profiles~~ simultaneously.

This study finds that tropical cyclones substantially increase TTL clouds. These TTL clouds occur frequently above tropical cyclones, ~~most of which are mostly as~~ non-convective high clouds (type CI) (above a clear troposphere (CI category, Fig. 4 (b)). This distribution of high clouds is consistent with in-situ aircraft observations (e.g., Jensen et al., 2013). Our finding emphasizes that the occurrence of ~~the~~ TTL cloud is ~~37.2%~~ 0.372 on average (Fig. 3 (a) and Fig.3(a)) over within the 2000 km \times 2000 km cyclone-centered composite domain, highlighting the importance of tropical eyelone cyclones in generating TTL clouds. In contrast to the horizontally extensive occurrence of TTL ~~clouds, the cloud cover~~ TTL cloud ice is most concentrated near the cyclone center (Fig. 3 (c) and Fig. 4 (a)), as ~~the a~~ result of direct overshooting convective overshooting and detrainment (Fig. 4 (c)). Furthermore, we find ~~the northwest that the northwestern quadrant~~ of the composite domain is less impacted by cyclones Fig. 3 (b,j). There is also a persistent southwest preference in TTL cloud ice and DCCs.

~~The results produced by the synergistic retrieval (Fig.10 (b)) suggest that cyclones mostly hydrate the atmospheric column above them. Above overshooting deep convective clouds, the column-integrated water vapor above 16 km is found to be 40 % higher than the local climatology. Both MLS v4.2 and the joint AIRS-DARDAR method are used to evaluate the impact of tropical cyclones on temperature and water vapor by compositing these fields as a function of radial distances to cyclone centers (Fig. ?? (b)). Substantial hydration is also found above clouds located beneath 16 km (NTTL). We suspect that this is likely from advected moist plumes from overshooting injection, though we are unable to prove our suspicions at this time. After isolating different cloud categories, dehydration is only found above non-overshooting TTL clouds (TTL-OTHERs) which are coincidentally associated with colder temperatures than other cloud categories (Fig7). 9 and ??). The coexistence of dehydration (as opposed to the moistening above other cloud categories), cold anomalies, and non-overshooting TTL clouds suggests that in this situation water vapor is likely deposited onto ice particles. Differences between the products are noticed in this study and they can arise for several reasons. First, contamination of cloud may cause artifacts in MLS v4.2 product, especially in temperature, that may not be effectively screened out by the cloud flag of the product (Schwartz et al., 2008; Livesey et al., 2017). Second,~~

595 sampling differences (MLS is off-nadir while AIRS, CPR, and CALIOP are nadir-looking) caused by instrument viewing geometry and the selection of samples can be substantial (see Fig. 5). Due to issues caused by cloud contamination, any MLS FOVs containing high cloud are excluded in this study for both temperature and water vapor. The implication of the joint AIRS-DARDAR method, however, exclusively selects FOVs that contain thick high clouds to perform the retrieval. Hence, the thermodynamic conditions of samples with or without high clouds can lead to large differences in the constructed cyclone
600 composites. Third, the horizontal resolution of the joint AIRS-DARDAR method is at least ten times finer than MLS. As a result, the joint AIRS-DARDAR method better captures the horizontal distribution pattern (Feng et al., 2021). Last, compared to MLS, the joint AIRS-DARDAR method has higher precision and vertical resolution for temperature but lower precision and vertical resolution for water vapor.

A Hence, the joint AIRS-DARDAR method is more advantageous in evaluating temperature fields related to tropical cyclone
605 events. Figure 8 shows a noticeable pattern of ~~vertically oscillating temperature anomalies~~, which ~~vertically oscillating temperature anomalies above tropical cyclones that lifts the cold-point tropopause level to higher altitudes,~~ ~~is found above eyclones~~. After investigating the cloud radiative effects in Section 4, we find that the signs of the temperature anomaly agree well with cloud effects on radiative heating rates, for example, the in-cloud warming (below the 0.01 g/m³ IWC contour in Figure Fig. 8 (a) and Figure Fig. 12 (d)) due to shortwave heating and ~~the~~ cloud-top cooling due to longwave cooling. The
610 cooling-environment Environmental cooling above clouds may also facilitate the formation of TTL clouds that ~~depletes deplete~~ moisture from the ~~eyclone detrainment detrainment of tropical cyclones~~, as indicated by the drier TTL over non-overshooting clouds. The cooling effect of tropical cyclones on cold-point ~~temperature temperatures~~ also implies the importance of deep ~~convections convection~~ in modulating the stratospheric water vapor, so that a strong linkage between stratospheric water vapor and cold-point temperature, as noted by Randel and Park (2019), cannot preclude the role of convection in water vapor
615 variability.

The joint AIRS-DARDAR method is also used to investigate overall (de)hydration above overshooting deep convective clouds and other non-overshooting clouds. Figure 8 (b) suggests that cyclones mostly hydrate the atmospheric column above them. Above overshooting deep convective clouds, the LIWV is found to be 40 % higher than the local climatology (Fig. 10 (b)). Substantial hydration is also found above clouds located beneath 16 km (NTTL). We suspect that this is likely
620 from advected moist plumes from overshooting injection, though we are unable to prove these suspicions at this time. After isolating different cloud categories, dehydration is only found above non-overshooting TTL clouds (TTL-OTHERs) which are coincidentally associated with colder temperatures than other cloud categories (Fig. 9 and 10). The coexistence of dehydration (as opposed to the moistening above other cloud categories), cold anomalies, and non-overshooting TTL clouds suggests that in this situation water vapor is likely deposited onto ice particles.

625 By comparing the nearest thermodynamic profiles from the ERA5 reanalysis (Fig. 8 (c,f)) to the synergistic retrieval (Fig. 8 (a,d)), we find that the cold anomaly in ERA5 is at a lower altitude, which is partially attributable to ~~the~~ biases in cloud ice in the reanalysis. The moistening ~~signal signals~~ around 80 hPa, as detected by the synergistic retrieval and MLS (Fig. 8 (d,e)) ~~is~~, are not shown in ERA5. These results suggest that the above-cyclone water vapor in ~~the reanalysis product reanalysis products~~

may be susceptible to the ~~convective parameterization of the model in simulating ability of models to simulate~~ cloud ice and
630 temperature ~~using convective parameterizations~~ (Wright et al., 2020).

Furthermore, we find that the cloud radiative effect is well-differentiated by BT_{1231} . Clouds heat the TTL via radiation when BT_{1231} shows a warm anomaly and cool the TTL when BT_{1231} shows a cold anomaly. Radiative cooling prevails above DCCs and thick anvils, which greatly reduce BT_{1231} . Radiative warming becomes more noticeable away from the cyclone center over thin cirrus. The radiative cooling anomaly further impacts the diabatic heating budget above ~~the cyclones, thus suppressing the~~
635 ~~tropical cyclones, suppressing~~ diabatic ascent and ~~transportation of air masses~~ ~~air mass transport across isentropic surfaces~~ to higher altitudes. It remains unclear how ~~the~~ ~~this~~ suppressed diabatic ascent, together with the strong horizontal divergence created by the pressure gradient above the cyclone, ~~can affect the~~ ~~affects~~ stratosphere-tropopause exchange and the water vapor budget. To elucidate this effect in the trajectory modeling in future work, it will require the use of instantaneous radiative heating computed from deep convection-perturbed TTL thermodynamic conditions (temperature, humidity, and cloud), as
640 opposed to climatologic or reanalysis heating profiles that do not properly represent the convective perturbations.

Finally, we would like to highlight the advantages of the synergistic method in retrieving the above-cloud ~~thermodynamic~~ conditions. This method takes advantage of collocated infrared hyperspectra and active sensors and is capable of retrieving temperature and water vapor ~~under for~~ overcast cloud conditions, ~~which is~~. ~~These features are~~ highly complementary to other datasets, including MLS v4.2 and AIRS L2 v6, that are limited to ~~the clear-sky~~ ~~condition~~ ~~conditions~~. So far, this approach
645 ~~is only has only been~~ applied to limited samples in the vicinity of tropical cyclones. It can be applied to other tropical and extra-tropical convective events, with potential implementation in other hyperspectral infrared sounders, ~~e.g., such as~~ IASI (Infrared Atmospheric Sounding Interferometer), CrIS (Cross-track Infrared Sounder), IRS (Infrared Spectrometer), and GIIRS (Geostationary Interferometric Infrared Sounder), to provide thermodynamic information over deep convective clouds on a global scale in future research.

650 *Author contributions.* YH conceived the cloud-assisted retrieval idea; JF implemented this idea with improvements using A-Train measurements. JF and YH co-designed the study of the tropical cyclone impacts and collectively wrote this paper.

Competing interests. The authors declare that they have no conflict of interest.

Acknowledgements. We thank ~~Jonathon Wright~~, Xun Wang, Kevin Bloxam, Lei Liu, ~~Louis Rivoire~~, and two anonymous reviewers for their constructive comments. This work is supported by grants from the Canadian Space Agency (16SUASURDC and 21SUASATHC)
655 and the Natural Sciences and Engineering Research Council of Canada (RGPIN-2019-04511). JF acknowledges the support of a Milton Leong Graduate Fellowship of McGill University. We thank Natalie Tourville for making the TC overpass dataset publically accessible (<https://adelaide.cira.colostate.edu/tc/>). We thank ICARE Data and Services Center (<http://www.icare-lille1.fr>) and Dr. Julien Delanoë for access to the DARDAR product.

Appendix A: Joint AIRS-DARDAR retrieval algorithm

660 ~~Feng and Huang (2018)~~ [Feng and Huang \(2018\)](#) applied a cloud-assisted retrieval to AIRS L1B infrared radiance from FOVs filled with deep convective clouds, assuming a blackbody cloud top. This method retrieves ~~the~~ atmospheric temperature and humidity [profiles](#) above the cloud top as described in Section 2.1 and ~~it can especially take advantage of~~ [is especially advantageous for](#) overcast conditions during tropical cyclone events. An updated version of this retrieval method ~~is~~ [has been](#) validated by Feng et al. (2021) ~~via~~ [using](#) simulation experiments and is adopted here. We briefly describe this retrieval method below and interested readers can find more details of this retrieval method from Feng et al. (2021).

In this method, we retrieve atmospheric states x that ~~includes~~ [include](#) temperature, humidity, ~~and~~ ice water content (IWC), [and effective radius](#) as an optimal estimation (Rodgers, 2000) that combines the *a priori* of x and the observation vector, y . The relationship between the state vector and the observation vector is expressed as:

$$\begin{aligned}
 y &= F(x_0) + \frac{\partial F}{\partial x}(x - x_0) + \varepsilon \\
 670 \quad &= y_0 + K(x - x_0) + \varepsilon
 \end{aligned} \tag{A1}$$

Where F is the forward model, K is the ~~jaacobian~~ [Jacobian](#) matrix, which is a first-order linear approximation of F , and ε is the residual. x_0 is the first guess, for which we use the mean of the *a priori*. Following the synergistic retrieval method (Feng et al., 2021), additional observation vectors are added, so that y is formed as $[y_{rad}, y_{iwc}, y_{Re}, y_{atm}]$. y_{rad} is the infrared hyperspectra from [the](#) AIRS L1B product, for which 1109 channels are selected, based on the radiometric quality of each channel. This rigorous channel selection also excludes ~~O3~~ [O3](#) absorption channels (980-1140 cm^{-1}), ~~CH4~~ [CH4](#) absorption channels (1255-1355 cm^{-1}), and shortwave infrared channels (2400-2800 cm^{-1}). y_{iwc} is a 2-km vertical IWC profile from [the](#) DARDAR-Cloud product, from 1.5 km below the DARDAR-identified cloud top to 0.5 km above it, ~~and~~ [. \$y_{Re}\$ is the effective radius, which holds constant through vertical layers of an atmospheric column.](#) y_{atm} is the temperature and humidity profile from the nearest ERA5 reanalysis product (hourly, 0.25×0.25). The *a priori* dataset is obtained from [the](#) AIRS L2 ~~v6~~ [supplementary product from supplementary product for temperature and water vapor and from the DARDAR-Cloud product for IWC and effective radius using data from](#) 2006 to ~~2016~~ [2014](#) in the Northern part of the West Pacific.

The forward model to convert the atmospheric states to y_{rad} is a radiative transfer model, the line-by-line version of MODerate spectral resolution TRANsmittance (MODTRAN 6.0 Berk et al., 2014). [Following Feng et al. \(2021\), user-defined extinction coefficients, single-scattering albedo, and asymmetry factor are input to MODTRAN, assuming vertically uniform optical properties \(per unit ice mass\) and solid-column crystal habit. Forward model uncertainties caused by this assumption is evaluated in Feng et al. \(2021\) and is around 0.1 K in the mid-infrared.](#) To relate x to y_{iwc} and y_{atm} , the forward model and the corresponding Jacobian matrix work as a linear interpolation matrix (~~Turner and Blumberg, 2018; Feng et al., 2021~~) ([Bowman et al., 2006; Feng et al., 2021](#)).

Using the Gaussian-Newton method, the best estimate of x , \hat{x} , is iteratively solved as:

$$\begin{aligned}
 690 \quad \hat{x}_{i+1} &= x_0 + (K_i^T S_\varepsilon^{-1} K_i + S_a^{-1})^{-1} K_i^T S_\varepsilon^{-1} [y - F(\hat{x}_i) + K_i(\hat{x}_i - x_0)] \\
 \hat{x}_{i+1} &= x_0 + (K_i^T S_\varepsilon^{-1} K_i + S_a^{-1})^{-1} K_i^T S_\varepsilon^{-1} [y - F(\hat{x}_i)] + A(\hat{x}_i - x_0)
 \end{aligned} \tag{A2}$$

Where the subscript i refers to the i th time step. S_a and S_ε are the covariance matrix of the *a priori* dataset and the observation vector, respectively, which are constructed the same as in Feng et al. (2021). More specifically, ~~the S_ε for y_{IWC}~~ is a diagonal matrix, ~~containing the square of the~~. The diagonal elements of S_ε for y_{rad} contain the sum of the square of radiometric noise of the instrument and the forward model uncertainty. For y_{IWC} , they contain the square of a doubling of posterior uncertainty of the IWC profile which is provided by the DARDAR-Cloud product at every measurement location and vertical level. For y_{B_c} , they contain the square of a doubling of posterior uncertainty of the effective radius of a vertical layer where optical depth measured from the cloud top reaches unity (Feng et al., 2021). The S_ε for y_{atm} is denoted as S_{atm} ; it contains the square of a doubling of the root-mean-square difference between collocated ERA5 and MLS v4.2 ~~product products~~ at every vertical level of ERA5. These uncertainty estimations are amplified in order to account for uncertainties caused by differences in the size and location of FOVs of different instruments.

The A in Eq. ~~A2-A3~~ is referred to as averaging kernel. Given a ‘truth’ state vector that $F(x_t) = y$, it links the truth state to the retrieved state, so that:

$$\hat{x} - x_0 = A(x_t - x_0). \quad (\text{A3})$$

Therefore, it regulates the vertical shape of the posterior estimation.

The iteration converges when:

$$(\hat{x}_{i+1} - \hat{x}_i)^T S (\hat{x}_{i+1} - \hat{x}_i) \ll N, \quad (\text{A4})$$

where ~~N~~ is the dimension of the state vector, and S is the posterior covariance matrix, which is computed combining the covariance matrix of *a priori* and observation vector:

$$S = (S_a^{-1} + K^T S_\varepsilon^{-1} K)^{-1} \quad (\text{A5})$$

Therefore, the ~~uncertainty in the retrieved state converges to \hat{x} is with an uncertainty range~~ equivalent to the square root of the diagonal element of the posterior covariance matrix S .

Feng et al. (2021) used a ~~system~~-simulation experiment to evaluate a synergistic retrieval approach that combines infrared spectra (y_{rad}) with another observation vector that includes the IWC product from collocated observation vector, denoted as y_{IWC} , and additional atmospheric observations, denoted as y_{atm} . In this simulation experiment, the ‘truth’ atmospheric condition is simulated from a cloud-resolving model during a tropical cyclone event. We mimic the infrared spectra from AIRS observation by adding synthetic noise to the forward model simulated infrared radiances that follow the spectral response function of AIRS. The IWC observation is simulated by perturbing the ‘truth’ IWC profile following the mean posterior uncertainty range provided by the DARDAR-Cloud product within 1000 km from cyclone centers. Therefore, the simulation experiment is designed to evaluate the realistic retrieval performance above thick upper-tropospheric clouds using AIRS L1B and DARDAR-Cloud ~~product products~~, with the same S_ε for the observation vectors.

The synergistic retrieval performed here is similar to Case 4 in Feng et al. (2021); the only differences are in the *a priori* dataset and the y_{atm} , which Feng et al. (2021) constructed hypothetically using numerical model simulation. To examine the

capacity of the retrieval method in revealing the realistic thermodynamic conditions, a simulation experiment similar to Feng et al. (2021) is performed here, using the *a priori* dataset and S_ϵ we introduced earlier. Figure A1-A1 shows the horizontal distribution of temperature and water vapor at 81 hPa, as well as the ~~column-integrated water vapor (CIWV, between 100 to 70 hPa)~~ integrated water vapor above 16 km from the simulated ‘truth’, the prior, the nearest ERA5 (y_{atm}), and the posterior of the retrieval. In ~~Figure A1~~ Fig. A1, the posterior shows a noticeable improvement compared to the prior and y_{atm} in reducing the mean biases and root-mean-square-error (RMSE). As a result, the posterior reveals the spatial feature of the ‘truth’, namely a moister and colder cyclone center.

According to Eq. ~~A4 and A5 and A6~~, the precision of this synergistic retrieval algorithm is given by the posterior uncertainty S , which is shown in ~~Figure A2~~ Fig. A2. The posterior uncertainty is within 1 K in temperature and is around 0.5 ppmv in water vapor around 80 hPa. While the uncertainty in IWC is equivalent to the DARDAR-Cloud product, the simulation experiment conducted by Feng et al. (2021) showed that the retrieval ~~can~~ is able to reduce the mean biases and RMSE in collocated IWC products caused by issues such as footprint mismatch.

Compared to other current satellite observational products in the UTLS, this retrieval has several advantages. First, the relatively small sampling footprint (15 km, the same as the size of the AIRS instantaneous FOV in the nadir) compared to limb-viewing sounders (>100 km) is beneficial for capturing small-scale variability directly impacted by deep ~~convections~~ convection. Second, the ability to retrieve temperature and water vapor above storms simultaneously. Third, the ability to retrieve atmospheric profiles near the cloud top. The simulation experiment conducted by Feng et al. (2021) evidenced that the synergistic method is capable of sounding the temperature profile near and slightly below the cloud top (within cloud optical depth of 1), while other products may not perform all-sky retrieval (AIRS L2, Susskind et al., 2003) or may be degraded by cloud presence (MLS v4.2 Schwartz et al., 2008; Livesey et al., 2017).

As depicted in the simulation experiment, the synergistic retrieval reveals the spatial variation in temperature and humidity. The retrieval is sensitive to the vertical variation of temperature (Fig. ~~A3 A3~~ (a,b)) but is not as sensitive to the vertical variation of water vapor (Fig. ~~A3 A3~~ (c,d)). The ~~coarse resolution of the~~ vertical resolution of water vapor retrieval is ~~due to the coarse~~ because the mid-infrared channels are less sensitive to the dry stratosphere, leading to a strong smearing effect of the averaging kernel (~~Feng et al., 2021~~) (Feng and Huang, 2018). This smearing effect is illustrated in ~~Figure A3~~ Fig. A3. In this test, we increase the temperature at every 20 hPa interval by 5 K as shown in ~~Figure A3~~ Fig. A3 (a), this corresponds to the term $x_t - x_0$ in Eq. ~~A3 A4~~. Similarly, the water vapor mixing ratio at every 20 hPa interval is increased by 50 % (considering the water vapor radiative effect is logarithmically scaled), as shown in ~~Figure A3~~ Fig. A3 (c). The responses from the averaging kernel are then calculated using Eq. ~~A3 A4~~, which are shown in ~~Figure A3~~ Fig. A3 (b,d) for temperature and water vapor, respectively. Figure ~~A3 A3~~ (a,b) shows that the retrieved temperature responds well to perturbation at different vertical ranges. However, ~~Figure A3~~ Fig. A3 (c,d) shows that the fine-scale water vapor perturbation would result in vertically broad, bottom-heavy water vapor anomalies in the retrieval. Nevertheless, the retrieval determines the changes in ~~CIWV~~ LIWV properly to detect (de)hydration. This is verified by the tests illustrated in Fig. ~~A3 A3~~ (c). Here, we prescribe random hydrations or dehydrations in randomly selected 20 hPa thick layers between 20 ~~to~~ and 100 hPa, following the same pattern in ~~Figure~~

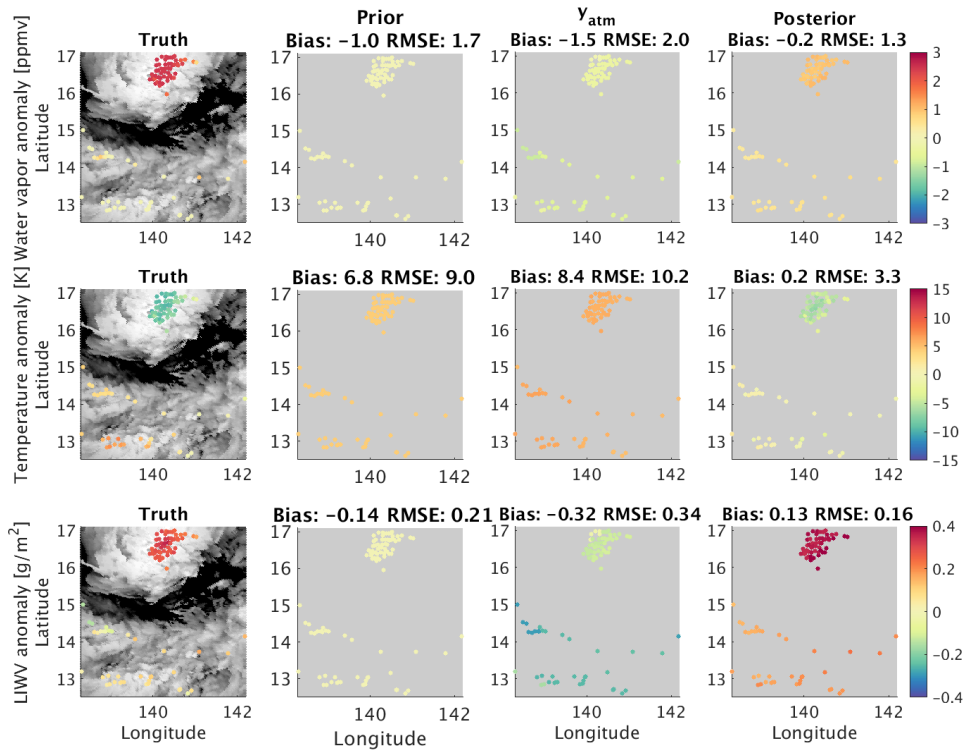


Figure A1. Horizontal distributions of the anomalies, defined as the deviation from the all-sky mean of the simulation field, in water vapor (in the units of ppmv, upper panels), temperature (in the units of K, middle panels) at 81 hPa, and column-layer integrated water vapor between 110 and 70 hPa (in the units of g/m^2 , lower panels). The truth fields are shown in the first column, with its background grey-shaded for BT_{1231} . The other columns show the distribution in the prior, nearest ERA5 (y_{atm}), and the posterior of the retrieval.

A3Fig. A3 (c), for 1000 cases. We find that the CIWV-LIWV changes produced by averaging kernel approach the truth better at higher altitudes, suggesting that the retrieval is more sensitive to perturbations at higher altitudes.

760 To evaluate the effects of cyclones on water vapor, samples above cyclones are compared to the climatology computed from the multi-year monthly mean of MLS data at the same grid as the retrieval samples. To remove the systematic bias caused by the higher vertical resolution of the MLS product, the MLS climatology is converted to the same vertical resolution using the averaging kernel of the synergistic retrieval, following Equation A3-Eq. A. The mean of the converted climatology profiles at retrieved sample locations is shown in Figure-Fig. 9 (b) black line, while the mean of retrieved water vapor anomalies in
 765 comparison with this converted climatology is shown in Figure-Fig. 8 (d) and Figure-Fig. 9 (d). These anomalies measure the impacts of cyclones. We note that this bias correction procedure affects the vertical structure of anomaly in water vapor, but has a negligible impact on the anomaly in CIWV-LIWV. Therefore, the conclusion on the hydration and dehydration impacts as shown in Figure-??-Fig. 10 are robust.

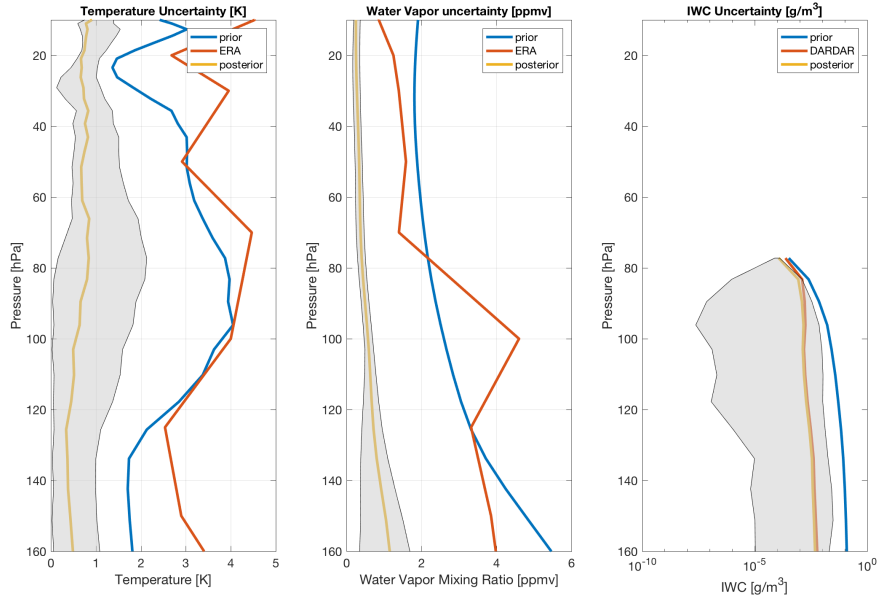


Figure A2. Uncertainties in temperature, water vapor mixing ratio, and IWC, estimated from the average of 2735 retrieved profiles with varied cloud top heights. Blue, red, and yellow curves show uncertainties of the prior (S_a), the ERA5 (S_{model}), and the posterior (S_{post}), respectively. The grey shaded area is the range of posterior uncertainties.

Appendix B: Binary classification of overshooting deep convective clouds

770 Similar to previous studies (Aumann and Ruzmaikin, 2013), we investigate BT of window channel at wavenumber 1231 cm^{-1} (BT_{1231}) and water vapor absorption channel at wavenumber 1419 cm^{-1} (BT_{1419}). In this section, we use collocated AIRS ~~radiances-observation-and-DARDAR-IWC~~ radiance observations and the DARDAR-Cloud product to evaluate the two metrics quantitatively and to identify the best threshold for determining the DCC-OTs.

As shown in Fig. B1, the distributions of BT_{1231} and ΔBT of overshooting DCCs resemble the Gaussian distribution in
 775 the intervals of ~~[210-185~~ [210] K and [-2 12] K, respectively. To find the optimized threshold for DCC-OT classification, we calculate the accuracy and the f1 score of DCC-OT classification combining $BT_{1231} \leq \varepsilon_{BT}$ and $\Delta BT \geq \varepsilon_{\Delta BT}$. The accuracy (α) and the f1 score ($F1$) are defined as:

$$\alpha = \frac{TP + TN}{TP + FP + FN + TN};$$

$$P = \frac{TP}{TP + FP};$$

$$R = \frac{TP}{TP + FN};$$

$$F1 = 2 \times \frac{R \times P}{R + P};$$
(B1)

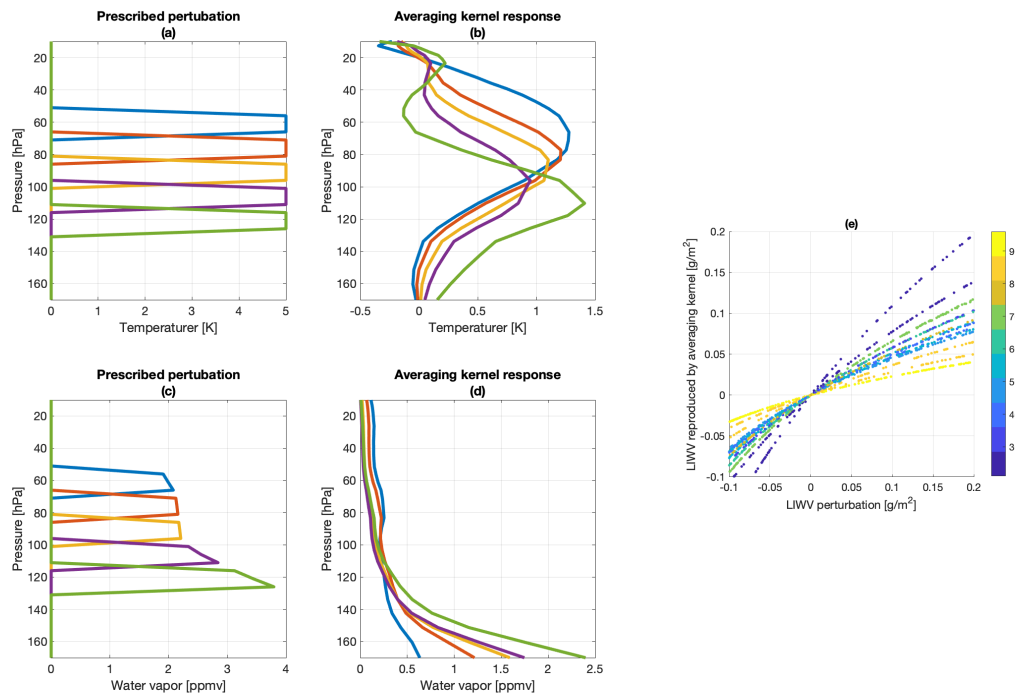


Figure A3. Averaging kernel responses to temperature and water vapor perturbation in thin layers. (a) Prescribed perturbation and (b) the response of averaging kernel in temperature [K]. (c) Prescribed perturbation and (d) the response of averaging kernel in water vapor [ppmv]. (e) $\epsilon_{LIWV-LIWV}$ perturbation [g/m^2] between 100 to 20 hPa reproduced by averaging kernel, color-coded for vertical pressure intervals (hPa) where the perturbation is prescribed.

780 Where the TP, TN, FP, and FN is-are the number of true positive, true negative, false positive, and false negative, respectively. While the P and R represent the precision and recall (equivalent with true positive rate) of this classification, the f1 score considers both by a harmonic average of the two factors.

As indicated by Fig. B1 (c), the accuracy of the classification gets around 0.985 when $\epsilon_{BT} \leq 204$ K or $\epsilon_{\Delta BT} \geq 2$ K. However, this high accuracy is partly a result of a small sample size from DCC-OT compared to the total. The f1 score is
 785 therefore used instead. The maximum $F1$ appears when $\epsilon_{BT} = 203$ K and $\epsilon_{\Delta BT} = 1$ K, although adding $\epsilon_{\Delta BT}$ criterion only increase $F1$ by 0.0004 which is considered to be negligible here. Using $\epsilon_{BT} = 203$ K leads to an FP rate at 0.008 and an FN rate at 0.323. Fig. Figure B1 (b) shows that the FP mainly comes from MIX and CI; their cold brightness temperature signal indicates sources from thick anvil cloud near the edge of the DCC system.

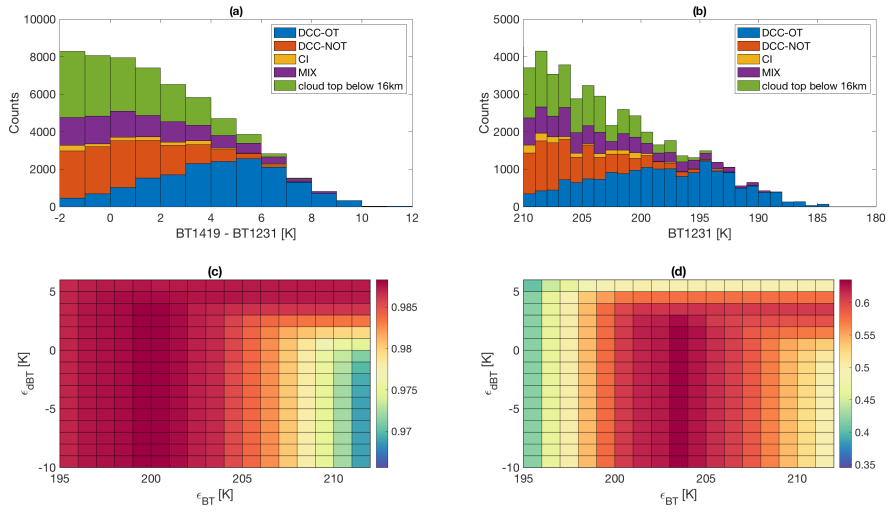


Figure B1. Distribution of (a) $BT_{1419} - BT_{1231}$ and (b) BT_{1231} of AIRS FOVs ~~under~~ for four TTL cloud categories and NTTLs (cloud top below 16 km). (c) The accuracy (Eq.1, α) and (d) f1 score ($F1$) of the DCC-OT classification using $BT_{1231} \leq \epsilon_{BT}$ and $BT_{1419} - BT_{1231} \geq \epsilon_{\Delta BT}$ criterion.

References

- 790 Anderson, J. G., Wilmouth, D. M., Smith, J. B., and Sayres, D. S.: UV dosage levels in summer: Increased risk of ozone loss from convectively injected water vapor, *Science*, 337, 835–839, 2012.
- Anthes, R. A., Bernhardt, P., Chen, Y., Cucurull, L., Dymond, K., Ector, D., Healy, S., Ho, S.-P., Hunt, D., Kuo, Y.-H., et al.: The COSMIC/FORMOSAT-3 mission: Early results, *Bulletin of the American Meteorological Society*, 89, 313–334, 2008.
- Aumann, H. and Ruzmaikin, A.: Frequency of deep convective clouds in the tropical zone from 10 years of AIRS data, *Atmospheric Chemistry and Physics*, 13, 10795, 2013.
- 795 Aumann, H., DeSouza-Machado, S., and Behrangi, A.: Deep convective clouds at the tropopause, *Atmospheric Chemistry and Physics*, 11, 1167, 2011.
- Austin, R. T., Heymsfield, A. J., and Stephens, G. L.: Retrieval of ice cloud microphysical parameters using the CloudSat millimeter-wave radar and temperature, *Journal of Geophysical Research: Atmospheres*, 114, 2009.
- 800 Avery, M. A., Davis, S. M., Rosenlof, K. H., Ye, H., and Dessler, A. E.: Large anomalies in lower stratospheric water vapour and ice during the 2015–2016 El Niño, *Nature Geoscience*, 10, 405–409, 2017.
- Berk, A., Conforti, P., Kennett, R., Perkins, T., Hawes, F., and Van Den Bosch, J.: MODTRAN® 6: A major upgrade of the MODTRAN® radiative transfer code, in: 2014 6th Workshop on Hyperspectral Image and Signal Processing: Evolution in Remote Sensing (WHISPERS), pp. 1–4, IEEE, 2014.
- 805 Bernath, P. F., McElroy, C. T., Abrams, M., Boone, C. D., Butler, M., Camy-Peyret, C., Carleer, M., Clerbaux, C., Coheur, P.-F., Colin, R., et al.: Atmospheric chemistry experiment (ACE): mission overview, *Geophysical Research Letters*, 32, 2005.
- Biondi, R., Ho, S.-P., Randel, W., Syndergaard, S., and Neubert, T.: Tropical cyclone cloud-top height and vertical temperature structure detection using GPS radio occultation measurements, *Journal of Geophysical Research: Atmospheres*, 118, 5247–5259, 2013.
- Bowman, K. W., Rodgers, C. D., Kulawik, S. S., Worden, J., Sarkissian, E., Osterman, G., Steck, T., Lou, M., Eldering, A., Shephard, M.,
810 et al.: Tropospheric emission spectrometer: Retrieval method and error analysis, *IEEE Transactions on Geoscience and Remote Sensing*, 44, 1297–1307, 2006.
- Brewer, A.: Evidence for a world circulation provided by the measurements of helium and water vapour distribution in the stratosphere, *Quarterly Journal of the Royal Meteorological Society*, 75, 351–363, 1949.
- Chahine, M. T., Pagano, T. S., Aumann, H. H., Atlas, R., et al.: AIRS: Improving weather forecasting and providing new data on greenhouse
815 gases, *Bulletin of the American Meteorological Society*, 87, 911, 2006.
- Comstock, J. M., Ackerman, T. P., and Mace, G. G.: Ground-based lidar and radar remote sensing of tropical cirrus clouds at Nauru Island: Cloud statistics and radiative impacts, *Journal of Geophysical Research: Atmospheres*, 107, AAC–16, 2002.
- Corti, T., Luo, B. P., Fu, Q., Vömel, H., and Peter, T.: The impact of cirrus clouds on tropical troposphere-to-stratosphere transport, *Atmospheric Chemistry and Physics*, 6, 2539–2547, 2006.
- 820 Delanoë, J. and Hogan, R. J.: A variational scheme for retrieving ice cloud properties from combined radar, lidar, and infrared radiometer, *Journal of Geophysical Research: Atmospheres*, 113, 2008.
- Delanoë, J. and Hogan, R. J.: Combined CloudSat-CALIPSO-MODIS retrievals of the properties of ice clouds, *Journal of Geophysical Research: Atmospheres*, 115, 2010.
- Deng, M., Mace, G. G., Wang, Z., and Okamoto, H.: Tropical Composition, Cloud and Climate Coupling Experiment validation for cirrus
825 cloud profiling retrieval using CloudSat radar and CALIPSO lidar, *Journal of Geophysical Research: Atmospheres*, 115, 2010.

- Deng, M., Mace, G. G., Wang, Z., and Lawson, R. P.: Evaluation of several A-Train ice cloud retrieval products with in situ measurements collected during the SPARTICUS campaign, *Journal of applied meteorology and climatology*, 52, 1014–1030, 2013.
- Dessler, A., Hints, E., Weinstock, E., Anderson, J., and Chan, K.: Mechanisms controlling water vapor in the lower stratosphere: “A tale of two stratospheres”, *Journal of Geophysical Research: Atmospheres*, 100, 23 167–23 172, 1995.
- 830 Dessler, A., Schoeberl, M., Wang, T., Davis, S., and Rosenlof, K.: Stratospheric water vapor feedback, *Proceedings of the National Academy of Sciences*, 110, 18 087–18 091, 2013.
- Feng, J. and Huang, Y.: Cloud-Assisted Retrieval of Lower-Stratospheric Water Vapor from Nadir-View Satellite Measurements, *Journal of Atmospheric and Oceanic Technology*, 35, 541–553, 2018.
- Feng, J., Huang, Y., and Qu, Z.: A simulation-experiment-based assessment of the retrieval of above-cloud temperature and water vapor using infrared hyper-spectrometers, *Atmospheric Measurement Techniques*, <https://doi.org/10.5194/amt-2020-518>, 2021.
- 835 Fetzer, E. J., Read, W. G., Waliser, D., Kahn, B. H., Tian, B., Vömel, H., Irion, F. W., Su, H., Eldering, A., de la Torre Juarez, M., Jiang, J., and Dang, V.: Comparison of upper tropospheric water vapor observations from the Microwave Limb Sounder and Atmospheric Infrared Sounder, *Journal of Geophysical Research: Atmospheres*, 113, n/a–n/a, <https://doi.org/10.1029/2008JD010000>, <http://dx.doi.org/10.1029/2008JD010000>, d22110, 2008.
- 840 Gettelman, A., Randel, W., Wu, F., and Massie, S.: Transport of water vapor in the tropical tropopause layer, *Geophysical research letters*, 29, 9–1, 2002.
- Gettelman, A., Weinstock, E. M., Fetzer, E. J., Irion, F. W., Eldering, A., Richard, E. C., Rosenlof, K. H., Thompson, T. L., Pittman, J. V., Webster, C. R., and Herman, R. L.: Validation of Aqua satellite data in the upper troposphere and lower stratosphere with in situ aircraft instruments, *Geophysical Research Letters*, 31, n/a–n/a, <https://doi.org/10.1029/2004GL020730>, <http://dx.doi.org/10.1029/2004GL020730>, 122107, 2004.
- 845 Henderson, D. S., L’Ecuyer, T., Stephens, G., Partain, P., and Sekiguchi, M.: A multisensor perspective on the radiative impacts of clouds and aerosols, *Journal of Applied Meteorology and Climatology*, 52, 853–871, 2013.
- Hersbach, H., Bell, B., Berrisford, P., Hirahara, S., Horányi, A., Muñoz-Sabater, J., Nicolas, J., Peubey, C., Radu, R., Schepers, D., et al.: The ERA5 global reanalysis, *Quarterly Journal of the Royal Meteorological Society*, 146, 1999–2049, 2020.
- 850 Holloway, C. E. and Neelin, J. D.: The convective cold top and quasi equilibrium, *Journal of the atmospheric sciences*, 64, 1467–1487, 2007.
- Holton, J. R. and Gettelman, A.: Horizontal transport and the dehydration of the stratosphere, *Geophysical Research Letters*, 28, 2799–2802, 2001.
- Holton, J. R., Haynes, P. H., McIntyre, M. E., Douglass, A. R., Rood, R. B., and Pfister, L.: Stratosphere-troposphere exchange, *Reviews of geophysics*, 33, 403–439, 1995.
- 855 Huang, Y., Ramaswamy, V., Huang, X., Fu, Q., and Bardeen, C.: A strict test in climate modeling with spectrally resolved radiances: GCM simulation versus AIRS observations, *Geophysical Research Letters*, 34, 2007.
- Huang, Y., Zhang, M., Xia, Y., Hu, Y., and Son, S.-W.: Is there a stratospheric radiative feedback in global warming simulations?, *Climate dynamics*, 46, 177–186, 2016.
- Iacono, M. J., Mlawer, E. J., Clough, S. A., and Morcrette, J.-J.: Impact of an improved longwave radiation model, RRTM, on the energy budget and thermodynamic properties of the NCAR community climate model, CCM3, *Journal of Geophysical Research: Atmospheres*, 105, 14 873–14 890, 2000.
- 860 Jensen, E., Ackerman, A., and Smith, J.: Can overshooting convection dehydrate the tropical tropopause layer?, *Journal of Geophysical Research: Atmospheres*, 112, 2007.

- Jensen, E. J., Pfister, L., Jordan, D. E., Fahey, D. W., Newman, P. A., Thornberry, T., Rollins, A., Diskin, G., Bui, T. P., McGill, M., et al.:
865 The NASA Airborne Tropical Tropopause Experiment (ATTREX), SPARC Newsletter, 41, 15–24, 2013.
- Jiang, J. H., Su, H., Zhai, C., Perun, V. S., Del Genio, A., Nazarenko, L. S., Donner, L. J., Horowitz, L., Seman, C., Cole, J., et al.: Evaluation
of cloud and water vapor simulations in CMIP5 climate models using NASA “A-Train” satellite observations, *Journal of Geophysical
Research: Atmospheres*, 117, 2012.
- Jiang, J. H., Su, H., Zhai, C., Wu, L., Minschwaner, K., Molod, A. M., and Tompkins, A. M.: An assessment of upper troposphere and
870 lower stratosphere water vapor in MERRA, MERRA2, and ECMWF reanalyses using Aura MLS observations, *Journal of Geophysical
Research: Atmospheres*, 120, 11–468, 2015.
- L’Ecuyer, T. S. and Jiang, J. H.: Touring the atmosphere aboard the A-Train, in: *AIP Conference Proceedings*, vol. 1401, pp. 245–256,
American Institute of Physics, 2011.
- Lee, K.-O., Dauhut, T., Chaboureau, J.-P., Khaykin, S., Krämer, M., and Rolf, C.: Convective hydration in the tropical tropopause layer
875 during the StratoClim aircraft campaign: pathway of an observed hydration patch, 2019.
- Livesey, N., Read, W., Wagner, P., Froidevaux, L., Lambert, A., Manney, G., Millán Valle, L., Pumphrey, H., Santee, M., Schwartz, M., et al.:
Version 4.2 x Level 2 data quality and description document, JPL D-33509 Rev. C, 2017.
- L’Ecuyer, T.: Level 2 fluxes and heating rates product process description and interface control document, v. 5, 2007.
- Mace, G. G., Zhang, Q., Vaughan, M., Marchand, R., Stephens, G., Trepte, C., and Winker, D.: A description of hydrometeor layer occurrence
880 statistics derived from the first year of merged Cloudsat and CALIPSO data, *Journal of Geophysical Research: Atmospheres*, 114, 2009.
- McErlich, C., McDonald, A., Schuddeboom, A., and Silber, I.: Comparing Satellite-and Ground-Based Observations of Cloud Occurrence
Over High Southern Latitudes, *Journal of Geophysical Research: Atmospheres*, 126, e2020JD033 607, 2021.
- Okamoto, H., Sato, K., and Hagihara, Y.: Global analysis of ice microphysics from CloudSat and CALIPSO: Incorporation of specular
reflection in lidar signals, *Journal of Geophysical Research: Atmospheres*, 115, 2010.
- 885 Olsen, E., Fetzer, E., Hulley, G., Manning, E., Blaisdell, J., Iredell, L., Susskind, J., Warner, J., Wei, Z., Blackwell, W., et al.:
AIRS/AMSU/HSB version 6 level 2 product user guide, Jet Propulsion Laboratory, Version, 1, 2013.
- Parkinson, C. L.: Aqua: An Earth-observing satellite mission to examine water and other climate variables, *IEEE Transactions on Geoscience
and Remote Sensing*, 41, 173–183, 2003.
- Partain, P.: Cloudsat ECMWF-AUX auxiliary data process description and interface control document, Cooperative Institute for Research in
890 the Atmosphere Rep, 2004.
- Plumb, R. A.: Stratospheric transport, *Journal of the Meteorological Society of Japan. Ser. II*, 80, 793–809, 2002.
- Qu, Z., Huang, Y., Vaillancourt, P. A., Cole, J. N., Milbrandt, J. A., Yau, M.-K., Walker, K., and de Grandpré, J.: Simulation of convective
moistening of the extratropical lower stratosphere using a numerical weather prediction model., *Atmospheric Chemistry & Physics*, 20,
2020.
- 895 Randel, W. and Park, M.: Diagnosing observed stratospheric water vapor relationships to the cold point tropical tropopause, *Journal of
Geophysical Research: Atmospheres*, 124, 7018–7033, 2019.
- Read, W. G., Lambert, A., Bacmeister, J., Cofield, R. E., Christensen, L. E., Cuddy, D. T., Daffer, W. H., Drouin, B. J., Fetzer, E., Froidevaux,
L., Fuller, R., Herman, R., Jarnot, R. F., Jiang, J. H., Jiang, Y. B., Kelly, K., Knosp, B. W., Kovalenko, L. J., Livesey, N. J., Liu, H.-C.,
Manney, G. L., Pickett, H. M., Pumphrey, H. C., Rosenlof, K. H., Sabouchi, X., Santee, M. L., Schwartz, M. J., Snyder, W. V., Stek, P. C.,
900 Su, H., Takacs, L. L., Thurstans, R. P., Vömel, H., Wagner, P. A., Waters, J. W., Webster, C. R., Weinstock, E. M., and Wu, D. L.: Aura
Microwave Limb Sounder upper tropospheric and lower stratospheric H₂O and relative humidity with respect to ice validation, *Journal*

- of Geophysical Research: Atmospheres, 112, n/a–n/a, <https://doi.org/10.1029/2007JD008752>, <http://dx.doi.org/10.1029/2007JD008752>, d24S35, 2007.
- 905 Rivoire, L., Birner, T., and Knaff, J. A.: Evolution of the upper-level thermal structure in tropical cyclones, *Geophysical Research Letters*, 43, 10–530, 2016.
- Rivoire, L., Birner, T., Knaff, J. A., and Tourville, N.: Quantifying the radiative impact of clouds on tropopause layer cooling in tropical cyclones, *Journal of Climate*, 2020.
- Robinson, F. and Sherwood, S.: Modeling the impact of convective entrainment on the tropical tropopause, *Journal of the atmospheric sciences*, 63, 1013–1027, 2006.
- 910 Rodgers, C. D.: *Inverse methods for atmospheric sounding: theory and practice*, vol. 2, World scientific, 2000.
- Romps, D. M. and Kuang, Z.: Overshooting convection in tropical cyclones, *Geophysical Research Letters*, 36, 2009.
- Saito, M., Iwabuchi, H., Yang, P., Tang, G., King, M. D., and Sekiguchi, M.: Ice particle morphology and microphysical properties of cirrus clouds inferred from combined CALIOP-IIR measurements, *Journal of Geophysical Research: Atmospheres*, 122, 4440–4462, 2017.
- Sampson, C. R. and Schrader, A. J.: The automated tropical cyclone forecasting system (version 3.2), *Bulletin of the American Meteorological Society*, 81, 1231–1240, 2000.
- 915 Sassen, K., Wang, Z., and Liu, D.: Cirrus clouds and deep convection in the tropics: Insights from CALIPSO and CloudSat, *Journal of Geophysical Research: Atmospheres*, 114, 2009.
- Schoeberl, M., Dessler, A., and Wang, T.: Simulation of stratospheric water vapor and trends using three reanalyses, *Atmospheric Chemistry and Physics*, 12, 6475–6487, 2012.
- 920 Schoeberl, M., Jensen, E., Pfister, L., Ueyama, R., Wang, T., Selkirk, H., Avery, M., Thornberry, T., and Dessler, A.: Water vapor, clouds, and saturation in the tropical tropopause layer, *Journal of Geophysical Research: Atmospheres*, 124, 3984–4003, 2019.
- Schoeberl, M. R., Jensen, E. J., Pfister, L., Ueyama, R., Avery, M., and Dessler, A. E.: Convective hydration of the upper troposphere and lower stratosphere, *Journal of Geophysical Research: Atmospheres*, 123, 4583–4593, 2018.
- Schubert, W. H. and McNoldy, B. D.: Application of the concepts of Rossby length and Rossby depth to tropical cyclone dynamics, *Journal of Advances in Modeling Earth Systems*, 2, 2010.
- 925 Schwartz, M., Lambert, A., Manney, G., Read, W., Livesey, N., Froidevaux, L., Ao, C., Bernath, P., Boone, C., Cofield, R., et al.: Validation of the Aura Microwave Limb Sounder temperature and geopotential height measurements, *Journal of Geophysical Research: Atmospheres*, 113, 2008.
- Schwartz, M. J., Read, W. G., Santee, M. L., Livesey, N. J., Froidevaux, L., Lambert, A., and Manney, G. L.: Convectively injected water vapor in the North American summer lowermost stratosphere, *Geophysical Research Letters*, 40, 2316–2321, 2013.
- 930 Solomon, S., Rosenlof, K. H., Portmann, R. W., Daniel, J. S., Davis, S. M., Sanford, T. J., and Plattner, G.-K.: Contributions of stratospheric water vapor to decadal changes in the rate of global warming, *Science*, 327, 1219–1223, 2010.
- Stephens, G. L., Vane, D. G., Tanelli, S., Im, E., Durden, S., Rokey, M., Reinke, D., Partain, P., Mace, G. G., Austin, R., et al.: CloudSat mission: Performance and early science after the first year of operation, *Journal of Geophysical Research: Atmospheres*, 113, 2008.
- 935 Sun, Y. and Huang, Y.: An examination of convective moistening of the lower stratosphere using satellite data, *Earth and Space Science*, 2, 320–330, 2015.
- Susskind, J., Barnet, C. D., and Blaisdell, J. M.: Retrieval of atmospheric and surface parameters from AIRS/AMSU/HSB data in the presence of clouds, *IEEE Transactions on Geoscience and Remote Sensing*, 41, 390–409, 2003.

- 940 Takahashi, H., Su, H., and Jiang, J. H.: Error analysis of upper tropospheric water vapor in CMIP5 models using “A-Train” satellite observations and reanalysis data, *Climate dynamics*, 46, 2787–2803, 2016.
- Tourville, N., Stephens, G., DeMaria, M., and Vane, D.: Remote sensing of tropical cyclones: Observations from CloudSat and A-Train profilers, *Bulletin of the American Meteorological Society*, 96, 609–622, 2015.
- Trepte, Q. Z., Minnis, P., Trepte, C., Sun-Mack, S., and Brown, R.: Improved cloud detection in CERES edition 3 algorithm and comparison with the CALIPSO vertical feature mask, in: *Proc. 13th Conf. on Atmospheric Radiation and Cloud Physics*, 2010.
- 945 Tseng, H.-H. and Fu, Q.: Temperature control of the variability of tropical tropopause layer cirrus clouds, *Journal of Geophysical Research: Atmospheres*, 122, 11–062, 2017.
- Turner, D. D. and Blumberg, W. G.: Improvements to the AERIOe thermodynamic profile retrieval algorithm, *IEEE Journal of Selected Topics in Applied Earth Observations and Remote Sensing*, 12, 1339–1354, 2018.
- Ueyama, R., Jensen, E. J., and Pfister, L.: Convective influence on the humidity and clouds in the tropical tropopause layer during boreal
950 summer, *Journal of Geophysical Research: Atmospheres*, 123, 7576–7593, 2018.
- Wang, Z., Vane, D., Stephens, G., and Reinke, D.: Level 2 combined radar and lidar cloud scenario classification product process description and interface control document, *JPL Rep*, 22, 2012.
- Waters, J. W., Froidevaux, L., Harwood, R. S., Jarnot, R. F., Pickett, H. M., Read, W. G., Siegel, P. H., Cofield, R. E., Filipiak, M. J., Flower, D. A., et al.: The earth observing system microwave limb sounder (EOS MLS) on the Aura satellite, *IEEE Transactions on Geoscience
955 and Remote Sensing*, 44, 1075–1092, 2006.
- Wetherald, R. and Manabe, S.: Cloud feedback processes in a general circulation model, *Journal of Atmospheric Sciences*, 45, 1397–1416, 1988.
- Winker, D., Pelon, J., Coakley Jr, J., Ackerman, S., Charlson, R., Colarco, P., Flamant, P., Fu, Q., Hoff, R., Kittaka, C., et al.: The CALIPSO mission: A global 3D view of aerosols and clouds, *Bulletin of the American Meteorological Society*, 91, 1211–1230, 2010.
- 960 WMO, W. M. O.: Definition of the tropopause, *WMO Bull.*, 6, 136, 1957.
- Wright, J. and Fueglistaler, S.: Large differences in reanalyses of diabatic heating in the tropical upper troposphere and lower stratosphere., *Atmospheric Chemistry & Physics*, 13, 2013.
- Wright, J. S., Sun, X., Konopka, P., Krüger, K., Molod, A. M., Tegtmeier, S., Zhang, G. J., and Zhao, X.: Differences in tropical high clouds among reanalyses: origins and radiative impacts., *Atmospheric Chemistry & Physics*, 2020.
- 965 Yang, Q., Fu, Q., and Hu, Y.: Radiative impacts of clouds in the tropical tropopause layer, *Journal of Geophysical Research: Atmospheres*, 115, 2010.
- Young, A. H., Bates, J. J., and Curry, J. A.: Application of cloud vertical structure from CloudSat to investigate MODIS-derived cloud properties of cirriform, anvil, and deep convective clouds, *Journal of Geophysical Research: Atmospheres*, 118, 4689–4699, 2013.